

Dual audible-range band gaps in three-dimensional locally resonant phononic crystalsKenny L. S. Yip^{✉*} and Sajeew John^{✉†}*Department of Physics, University of Toronto, 60 St. George Street, Toronto, Ontario, Canada M5S 1A7*

(Received 9 March 2023; revised 31 May 2023; accepted 2 June 2023; published 12 June 2023)

We describe a simple and transparent physical model for local acoustic resonances and their interactions in three-dimensional phononic crystals. The widely quoted point-mass-in-a-box representation of acoustic resonators is systematically generalized to an extended rigid body connected to massive springs, exhibiting multiple coupled local resonances. Millimeter-sized acoustic resonators over the audible frequency range typically consist of dense cores coupled to stiff shells through elastically soft material. When the local resonator is small compared to the acoustic wavelength, an elastostatic equilibrium approximation yields closed-form rational functions for its frequency-dependent, effective mass and moment of inertia. Our representation allows intuitive and quantitative analyses of the coupled acoustic modes of lattices of interacting resonators. The existence and the frequency range of local resonance band gaps are predicted by the concurrence of negative effective mass and moment of inertia. A large local resonance gap may occur in spectral proximity to a distinct gap arising from Bragg scattering. The band structure and density of states are determined by solving computationally inexpensive 6×6 matrix eigenvalue equations. These agree with the exact band structures obtained by finite-element method within 3.71%, 2.32%, and 2.38% errors for the simple cubic, body-centered cubic, and face-centered cubic arrangements of the resonators, respectively. Our model enables precise design of locally resonant phononic crystals with large dual band gaps spanning a significant fraction of the audible spectrum. By increasing the mass contrast between the core and the shell in spherical resonators, we demonstrate, using a specific phononic crystal, a local resonance band gap with 126.7% gap-to-midgap ratio. Our model is further extended to a lattice of dumbbell-shaped resonators, resulting in a dense collection of flat bands over a narrow, predetermined frequency range.

DOI: [10.1103/PhysRevB.107.214304](https://doi.org/10.1103/PhysRevB.107.214304)**I. INTRODUCTION**

Phononic crystals are periodic composites composed of several elastic materials. Early proposals concentrated on the existence of phononic band gaps, over which transmission of elastic waves is inhibited [1–4]. These conventional nonresonant phononic crystals rely on Bragg scattering of elastic waves, and require substantial sizes of the repeating units to exhibit its nontrivial phononic properties over the audible frequency range. In context, the wavelength of the A440 tuning pitch is about 1 m in air and 10 m in typical stiff solids. The scaling problem is solved by introducing local resonances in the unit cell. Liu *et al.* fabricated a three-dimensional, locally resonant sonic crystal, consisting of dense lead balls embedded in elastically soft silicone rubber. With a lattice constant of 1.55 cm, a subwavelength band gap from 400 to 600 Hz is achieved [5]. Locally resonant acoustic metamaterials render the possibilities of subwavelength manipulation of sound waves, from acoustic lens and collimators, to waveguides, polarization beam splitters, and vibration isolation devices [6–9].

Rapid and high-accuracy fabrication of three-dimensional, millimeter-sized acoustic metamaterials is increasingly viable under the technological advances in additive manufacturing

and direct laser lithography [10–13]. Relevant experimental studies have focused on nonresonant phononic crystals, with band gaps in the ultrasonic regime for millimeter-sized unit cells [11,14,15]. Precise and efficient representations of locally resonant acoustic metamaterials are essential to broaden the engineering applications over the audible frequency range. Matlack *et al.* proposed lumped element discrete models for a class of metamaterials with weakly interacting unit cells, referred to as “perturbative metamaterials” [16]. While the application was restricted to weakly interacting systems, the reduced order model faithfully reproduced various novel functionalities of metamaterials, such as negative refraction, zero group velocity, and topologically protected edge modes in certain two-dimensional, beam-hole metamaterials.

Previously, an effective inertia spring tensor (EIST) model was introduced to recapture the coupling between different types of local resonances [17,18]. It was applied to two-dimensional, locally resonant, acoustic materials with translational invariance along the axial direction. The predominant degrees of freedom, which describe the coupling between the resonators and the host medium, are the out-of-plane translation, in-plane translations in two orthogonal directions, and in-plane rotation. Since the sizes of the resonators are small compared to the acoustic wavelengths, an elastostatic analysis was utilized to derive analytical expressions of the effective mass and moment of inertia, as rational functions in the square of frequency [19]. On the other hand, a wave-vector-dependent spring tensor represents the generalized forces acting on the resonators by the host medium, as

*Corresponding author: lscopy@physics.utoronto.ca†john@physics.utoronto.ca

a result of the relative displacements between the resonators in the periodic medium. At a given wave vector, the acoustic eigenfrequencies and eigenmodes are described by a simple polynomial equation for the out-of-plane modes, and a 3×3 matrix eigenvalue equation for the in-plane modes.

In this paper, we extend the EIST model to three-dimensional, locally resonant, phononic crystals [18]. We elaborate the physics of frequency-dependent, effective inertia and provide a compact formula in terms of the determinants of the dynamical matrix. The representation is beyond the conventional mass-in-a-box physical picture, as it accommodates the possibilities of massive springs and multiply coupled local resonances through a general Hermitian inertia tensor. In three dimensions, the rigid-body degrees of freedom are the translations and rotations in three orthogonal directions. In general, the effective inertia tensor consists of the effective masses, moments of inertia, and certain off-diagonal couplings. We apply the EIST model to obtain the low-frequency acoustic band structures of spherically symmetric core-shell resonators, arranged in simple cubic (sc), body-centered cubic (bcc), and face-centered cubic (fcc) configurations. The resultant acoustic bands are accurately represented by our EIST model within 3.71%, 2.32%, and 2.38% errors for the sc, bcc, and fcc arrangements, respectively, compared to the finite-element method (FEM) results of the exact phononic crystals. In the EIST model, the eigenfrequencies and eigenmodes are governed by a computationally inexpensive 6×6 matrix equation, allowing efficient evaluation of total vibrational density of states. Moreover, complete band gaps, caused by local resonances, occur over comparable frequency intervals across lattice structures. In specific examples, with centimeter-sized lattice constants, we demonstrate local resonance gaps from 348 to 620 Hz for the sc lattice, from 337 to 621 Hz for the bcc, and from 336 to 621 Hz for the fcc. The corresponding Bragg gaps are from 1300 to 2800 Hz for the sc lattice, from 1000 to 3700 Hz for the bcc, and from 1000 to 3500 Hz for the fcc. All of these band edge frequencies scale inversely with the phononic crystal lattice constant. It is transparent in the EIST representation that a resonance gap occurs over the frequency range where the effective masses and moments of inertia are simultaneously negative. The same effective inertia tensor applies regardless of the differences of the lattice configurations, whereas the lattice effects are contained in the spring tensor. The first six bands below the resonance gaps correspond to coupled in-phase translational and rotational oscillations of the core and the shell. In the next six bands above the resonance gap, the shell and the core oscillate antiphase. The resonance gap between the in-phase and antiphase bands is likely very tolerant to lattice defects. Above the antiphase bands is the Bragg gap that is caused by the macroscopic resonance of the entire collection of local resonators and is sensitively dependent on the lattice arrangements.

The EIST model is ideally suited to the study of a lattice of local resonators and the interaction between different types of resonances across spatially separated units. Using the results of spherically symmetric core-shell resonators, we investigate an example with significant mass contrasts between the heavy core and the light shell. This leads to a complete, three-dimensional local resonance band gap of 126.7% gap-to-midgap ratio, just below the frequency range of the Bragg

gap. Both gaps occur at audible frequencies. This suggests the possibility of a broad range of acoustic wave control. We further apply the EIST model to dumbbell-shaped resonators, which require systematic generalizations to a complex Hermitian spring tensor and a nondiagonal effective inertia tensor. Through connecting two resonators with nearby resonant frequencies, we are able to deterministically engineer a dense collection of slow-sound flat bands sandwiched between two predetermined resonant frequencies. These examples demonstrate the efficacy of our EIST model in designing locally resonant phononic crystals for audible sound manipulations.

This paper is organized as follows. In Sec. II, we survey the elastodynamic equations and methods for solving the acoustic mode spectrum of phononic crystals. In Sec. III, we introduce the effective inertia spring tensor (EIST) model for three-dimensional phononic crystals, and determine general expressions of frequency-dependent effective inertia. In Sec. IV, we approximate the elastic components in resonators as massless springs to derive algebraic expressions of frequency-dependent, effective mass and moment of inertia of spherical resonators. In Sec. V, we apply our EIST model to simple cubic, body-centered cubic, and face-centered cubic lattices of spherical resonators. We compare the results of the EIST model with the finite-element method benchmark. In Sec. VI, we apply the EIST model to more complex resonators involving extreme mass contrasts and coupled local resonances. In Sec. VII, we discuss open questions and possible future directions. In Appendix A, we describe a convergent plane wave expansion scheme for three-dimensional phononic crystals in the presence of material discontinuities. In Appendix B, we analyze an exactly solvable effective mass model involving a massive spring. In Appendix C, we summarize the evaluation of the spring tensor by plane wave expansion. This goes beyond the nearest-neighbor approximation outlined in the main text. In Appendix D, we present the detailed elastostatic equilibrium calculation of the rotational modes in spherical core-shell resonators. Similarly, in Appendix E, details of the elasticity analysis of the translational modes in spherical core-shell resonators are provided. In Appendix F, we calculate the parameters required for the effective inertia tensor of a dumbbell-shaped resonator.

II. BACKGROUND

We begin with a brief review of linear elasticity theory and band structure calculation for a periodic elastic medium.

A. Linear elasticity

At a given position $\mathbf{x}=(x_1, x_2, x_3)$, the field $\mathbf{u}=(u_1, u_2, u_3)$ defines the displacement from the equilibrium of the infinitesimally small parcel of elastic material. The local deformation is given by the symmetric strain tensor ϵ_{ij} [20]:

$$\epsilon_{ij} = \frac{1}{2} \left(\frac{\partial u_i}{\partial x_j} + \frac{\partial u_j}{\partial x_i} \right). \quad (1)$$

Linear elasticity is assumed by dropping the nonlinear term $(1/2) \sum_k (\partial u_k / \partial x_i) (\partial u_k / \partial x_j)$.

A general elastic deformation can be decomposed into the superposition of a compressional deformation and a shear

deformation. For an isotropic, linear, elastic material, the elastic restoring forces are defined by two free elastic constants. Lamé first coefficient λ describes the tendency to resist volume change, whereas Lamé second coefficient μ is associated with the elastic restoring force to resist lateral distortion. The stress tensor σ_{ij} specifies the i component of the elastic force acting on a plane of unit area with the normal vector in the j direction, and is linearly proportional to the strain tensor ϵ_{ij} [20]:

$$\sigma_{ij} = C_{ijkl}\epsilon_{kl} = \lambda \text{Tr}(\vec{\epsilon})\delta_{ij} + 2\mu\epsilon_{ij}, \quad (2)$$

where $C_{ijkl} = \lambda\delta_{ij}\delta_{kl} + 2\mu\delta_{ik}\delta_{jl}$ is the fourth-order stiffness tensor, δ_{ij} is the Kronecker delta function, and Tr is the trace operator.

The dynamical field equation in an elastic material of density ρ is given by Newton's second law:

$$\rho \frac{\partial^2 u_i}{\partial t^2} = \frac{\partial \sigma_{ij}}{\partial x_j}. \quad (3)$$

For a finite force acting on each infinitesimal parcel, the stress tensor $\vec{\sigma}$ must be continuous everywhere. For an isotropic linear elastic solid, Eqs. (2) and (3) yield the elastodynamic equation

$$\rho \frac{\partial^2 \mathbf{u}_i}{\partial t^2} = \nabla \cdot (\mu \nabla \mathbf{u}_i) + \nabla \cdot \left(\mu \frac{\partial \mathbf{u}}{\partial x_i} \right) + \frac{\partial}{\partial x_i} (\lambda \nabla \cdot \mathbf{u}). \quad (4)$$

We express the displacement field in Cartesian coordinates: $\mathbf{u} = u_x \hat{\mathbf{x}} + u_y \hat{\mathbf{y}} + u_z \hat{\mathbf{z}}$. Monochromatic oscillation at angular frequency ω with temporal dependence $e^{-i\omega t}$ is assumed. The components of the displacement field are intricately coupled:

$$\frac{\partial}{\partial x} \left[(\lambda + 2\mu) \frac{\partial u_x}{\partial x} + \lambda \frac{\partial u_y}{\partial y} + \lambda \frac{\partial u_z}{\partial z} \right] + \frac{\partial}{\partial y} \left(\mu \frac{\partial u_x}{\partial y} + \mu \frac{\partial u_y}{\partial x} \right) + \frac{\partial}{\partial z} \left(\mu \frac{\partial u_x}{\partial z} + \mu \frac{\partial u_z}{\partial x} \right) + \rho \omega^2 u_x = 0, \quad (5a)$$

$$\frac{\partial}{\partial x} \left(\mu \frac{\partial u_x}{\partial y} + \mu \frac{\partial u_y}{\partial x} \right) + \frac{\partial}{\partial y} \left[\lambda \frac{\partial u_x}{\partial x} + (\lambda + 2\mu) \frac{\partial u_y}{\partial y} + \lambda \frac{\partial u_z}{\partial z} \right] + \frac{\partial}{\partial z} \left(\mu \frac{\partial u_y}{\partial z} + \mu \frac{\partial u_z}{\partial y} \right) + \rho \omega^2 u_y = 0, \quad (5b)$$

$$\frac{\partial}{\partial x} \left(\mu \frac{\partial u_x}{\partial z} + \mu \frac{\partial u_z}{\partial x} \right) + \frac{\partial}{\partial y} \left(\mu \frac{\partial u_y}{\partial z} + \mu \frac{\partial u_z}{\partial y} \right) + \frac{\partial}{\partial z} \left[\lambda \frac{\partial u_x}{\partial x} + \lambda \frac{\partial u_y}{\partial y} + (\lambda + 2\mu) \frac{\partial u_z}{\partial z} \right] + \rho \omega^2 u_z = 0. \quad (5c)$$

The dynamical equations obey cyclic permutation symmetry: $x \rightarrow y$, $y \rightarrow z$, and $z \rightarrow x$.

B. Acoustic band structure

By discrete translational symmetry, the solution to the dynamical equation (4) is a superposition of Bloch waves, which are plane waves multiplied by a function with the periodicity of the lattice (Bloch's theorem):

$$\mathbf{u}(\mathbf{r}, t) = \exp(i\mathbf{K} \cdot \mathbf{r} - i\omega_{\mathbf{K}} t) \sum_{\mathbf{G}} \mathbf{u}_{\mathbf{K}}(\mathbf{G}) \exp(i\mathbf{G} \cdot \mathbf{r}). \quad (6)$$

Here, \mathbf{K} denotes the Bloch wave vector. \mathbf{G} denotes a reciprocal lattice vector implied by the underlying lattice symmetry. $\mathbf{u}_{\mathbf{K}}(\mathbf{G})$ denotes the Fourier coefficient of the periodic modulation function. $\omega_{\mathbf{K}}$ denotes the eigenfrequency at the given wave vector.

A general approach to evaluating the eigenfrequencies is the plane wave expansion (PWE) method [1,2,21]. The displacement field and material parameters are expanded into Fourier series. Under the orthogonality and a proper truncation of the plane wave basis, the dynamical equations are transformed into a finite-dimensional matrix eigenvalue problem. Across the material boundary, while the strain tensor and material properties are discontinuous, the stress tensor is continuous for a finite force to act on each infinitesimal parcel. There is a well-understood analog in electromagnetism. Across the surface of a dielectric, while the normal component of the electric field and the dielectric constant are discontinuous, their product, the normal component of the electric displacement, is continuous. To ensure numerical convergence, Fourier series containing complementary

discontinuities are multiplied by the ‘‘inverse rule’’ [22–24]. Algebraic details of an efficient and convergent plane wave expansion scheme in three dimensions are provided in Appendix A. In a widely applied reduced Bloch mode expansion [25–27], the eigensolutions at a general \mathbf{K} point are approximated by linear superpositions of the eigenfunctions at high-symmetry \mathbf{K} points.

The finite-element method (FEM) is another well-established technique of numerically solving partial differential equations [28–32]. COMSOL MULTIPHYSICS equipped with Acoustics Module is a readily available commercial FEM software for eigenmode analysis of elastic structures. Throughout this paper, we benchmark the predictions of our model against the COMSOL FEM results.

The multiple scattering method originates from the superposition of single-scatterer wave solutions and the boundary conditions on the surface of the scatterers. The theory was first proposed for the calculations of electronic band structure of periodic solids, and is referred to as the Korringa-Kohn-Rostoker method (KKR method) [33–37]. Readers can refer to Appendix B in [17] and references therein for further discussion of the formulation of multiple scattering of partial waves in acoustic mode spectrum calculations of phononic crystals. Present applications are primarily limited to cylindrical scatterers in two dimensions and spherical scatterers in three dimensions. Such a method is relatively unpopular because it involves conditionally convergent lattice sums and nonlinear eigenvalue equations [38], compounded with an extensive use of special functions. In homogenization approaches, the entire elastic composite is treated as an effective medium [39–42], where the effective parameters are determined by empirically fitting with the transmission spectrum [5] or the

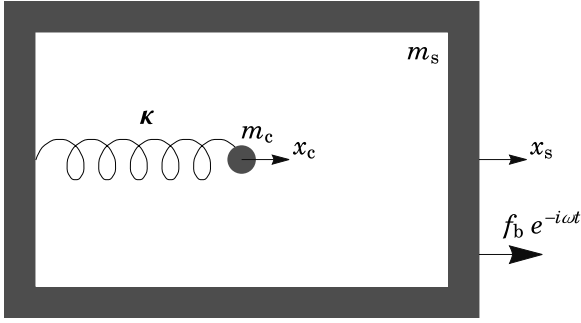


FIG. 1. A container of mass m_s is coupled to an interior mass m_c via a Hermitian coupling matrix κ . The displacements of the box and the core are x_s and x_c , respectively. The resonator is harmonically driven by an external force $f_b e^{-i\omega t}$.

phononic band structure [40,43]. A similar effective medium approach is the coherent potential approximation where the partial waves from a resonator are compared to a nonresonant, isotropic, replacement medium in the long-wavelength limit [43,44]. We also mention the transfer matrix method that specializes in one-dimensional and layered systems [45–47], as well as the variational method that utilizes the stationarity of a mixed functional of displacement and stress fields at the eigenmodes [48,49].

III. EFFECTIVE INERTIA SPRING TENSOR MODEL

The physical idea of the effective inertia spring tensor (EIST) model stems from Newton's second law and Hooke's law. Inertia is the ratio of the net external force to the acceleration. When extended to oscillatory systems, this gives rise to the concept of frequency-dependent, effective inertia. Hooke's law postulates a general linear relation between the displacement from equilibrium and the elastic restoring force. The microscopic formulation is the constitutive relation (2) between the strain and stress tensors, which is fundamental to the theory of linear elasticity. From a macroscopic perspective, there is also a linear map from a set of large-scale degrees of freedom to the associated generalized forces. This linear map leads to the concept of the spring tensor. It depends on the geometry and the stiffness parameters of the elastic material, but is insensitive to the interior of the objects that the spring couples to.

A. Effective inertia

Consider a box of mass m_s with displacement x_s , coupled to an interior mass m_c with displacement x_c through a Hermitian coupling matrix $\kappa = ((\kappa_{11}, \kappa_{21})^T, (\kappa_{12}, \kappa_{22})^T)$. The box responds to an external harmonic force $f_b e^{-i\omega t}$, and all the components oscillate at the same angular frequency ω . The setup is schematically shown in Fig. 1. The equations of motion are given by Newton's second law:

$$-m_s \omega^2 x_s = -\kappa_{11} x_s - \kappa_{12} x_c + f_b, \quad (7a)$$

$$-m_c \omega^2 x_c = -\kappa_{21} x_s - \kappa_{22} x_c. \quad (7b)$$

Equation (7b) is rearranged to obtain a frequency-dependent proportionality factor between the displacements of the box

and the core:

$$x_c = \left(\frac{-\kappa_{21}}{\kappa_{22} - m_c \omega^2} \right) x_s, \quad (8)$$

which is substituted into Eq. (7a) to yield

$$\left\{ \frac{1}{-\omega^2 (\kappa_{22} - m_c \omega^2)} [(\kappa_{11} \kappa_{22} - \kappa_{12} \kappa_{21}) - (m_c \kappa_{11} + m_s \kappa_{22}) \omega^2 + m_s m_c \omega^4] \right\} \ddot{x}_s = f_b. \quad (9)$$

The coefficient of the second time derivative of the displacement is interpreted as the frequency-dependent, effective mass $m_e(\omega)$ of the resonator:

$$m_e(\omega) = \frac{1}{-\omega^2 (\kappa_{22} - m_c \omega^2)} \begin{vmatrix} \kappa_{11} - m_s \omega^2 & \kappa_{12} \\ \kappa_{21} & \kappa_{22} - m_c \omega^2 \end{vmatrix}. \quad (10a)$$

In the special case when the internal coupling reduces to the Hooke's law for massless springs, $\kappa_{11} = \kappa_{22} = \kappa$ and $\kappa_{12} = \kappa_{21} = -\kappa$, the effective mass assumes the familiar form

$$m_e(\omega) = \frac{\kappa (m_c + m_s) - m_s m_c \omega^2}{\kappa - m_c \omega^2} = m_s \left[\frac{(\omega_*)^2 - \omega^2}{(\omega_0)^2 - \omega^2} \right], \quad (10b)$$

where ω_0 denotes the resonant frequency at which the effective mass diverges to infinity, and ω_* denotes the frequency at which the effective mass vanishes:

$$\omega_0 = (\kappa/m_c)^{1/2}, \quad (11a)$$

$$\omega_* = (\kappa/m_c + \kappa/m_s)^{1/2} = (\kappa/m_r)^{1/2}, \quad (11b)$$

where $m_r = m_c m_s / (m_c + m_s)$ is the reduced mass. The effective mass in Eq. (10a) is, in fact, nonsingular at $\omega = 0$. It is because $\det(\kappa) = \kappa_{11} \kappa_{22} - \kappa_{12} \kappa_{21}$ vanishes at zero frequency, which balances the ω^2 term in the denominator. The cancellation at zero frequency generally holds, as required by Newton's third law that the internal forces cancel out identically. An alternative interpretation is that uniform translational motion of the entire resonator in the absence of an external force is a normal mode at zero frequency.

More generally, for a resonator with n internal degrees of freedom x_i of inertia m_i , the coupling is represented by a $n \times n$ Hermitian matrix κ_{ij} . The determinant of the coupling tensor vanishes at zero frequency because all the internal forces cancel out exactly by Newton's third law. The equations of motion are governed by Newton's second law:

$$-m_i \omega^2 x_i = -\kappa_{ij} x_j + f_b \delta_{i1}. \quad (12)$$

The index $i = 1, 2, 3, \dots, n$, where $i = 1$ denotes the resonator shell that couples to the external harmonic force $f_b e^{-i\omega t}$. The frequency-dependent, effective mass $m_e(\omega)$ is

$$m_e(\omega) = \frac{\det(\kappa_{ij} - \delta_{ij} m_i \omega^2)}{-\omega^2 M_{11}}, \quad (13)$$

where \det denotes the determinant of a matrix and M_{11} denotes the determinant of the submatrix (first minor) of $(\kappa_{ij} - \delta_{ij} m_i \omega^2)$ obtained by deleting the first row and the first column associated with the shell's degree of freedom. The $n = 2$ case is shown explicitly in Eq. (10a). The assertion can

be proved using the cofactor expansions of determinant and matrix inverse. Assuming that the system is in mechanical equilibrium at rest [$\det(\kappa) = 0$], we cancel out the common ω^2 factors in the numerator and the denominator. Both the numerator and the denominator in Eq. (13) are degree $n - 1$ polynomials in ω^2 . It is customary to express the effective mass in terms of the zero-mass frequencies $\omega_{*,j}$ and the resonant frequencies $\omega_{0,j}$ with $1 \leq j \leq n - 1$, which are zeros of the numerator and the denominator in Eq. (13), respectively:

$$m_e(\omega) = m_1 \left(\prod_{j=1}^{n-1} \frac{\omega_{*,j}^2 - \omega^2}{\omega_{0,j}^2 - \omega^2} \right). \quad (14)$$

The zero-mass frequencies are the normal mode frequencies of the resonator, associated with the free vibrations. The effective mass of the resonator changes its sign across such frequencies, often signaling a transition from a stop gap to a pass band. On the other hand, the resonant frequencies are the normal mode frequencies of the interior of the resonator, when the resonator shell is spatially fixed. The effective mass diverges near the resonant frequencies because a small displacement of the shell implies substantially larger displacements of the interior masses. This generalized form allows efficient computation when the resonator has numerous internal degrees of freedom, or when the coupling matrix is frequency dependent. For example, as a massive spring carries momentum, the propagation of the disturbance from one end of the spring to another is no longer instantaneous. The relevant Hermitian coupling matrix is frequency dependent. Detailed treatment of the resonator with a massive spring is provided in Appendix B.

Similar order-reduction techniques are extensively applied in structural engineering under the notion of “dynamic condensation” [50,51]. The engineering applications mostly focused on simplifying the numerical finite-element method (FEM) computations for a variety of complex mechanical structures, such as vehicle-bridge system [52] and commercial transport aircraft [53]. In subsequent applications, we demonstrate the efficacy of the algebraic, frequency-dependent, effective inertia in analyzing acoustic modes of locally resonant phononic crystals.

B. Rod-in-a-box model

The effective inertia tensor acquires a pair of nonzero off-diagonal components, when the interior of a resonator is not symmetric about the center of the shell. The mass-in-a-box model with a pair of identical springs was studied [18]. We now consider a generalized rod-in-a-box model, depicted in Fig. 2, where the requirement of identical springs is relaxed. The resonator consists of a rigid box of mass m_s uniformly distributed along its left sidewall, and transverse moment of inertia I_s about its center of mass. All other walls are assumed to be massless. The box is coupled to a thin uniform interior rod of mass m_c and transverse center-of-mass moment of inertia I_c , through a pair of massless springs. The linear (angular) displacements of the shell and the core are denoted by x_s (ϕ_s) and x_c (ϕ_c), respectively. The springs, located at $(a + d)$ and $(a - d)$ from the center of the left sidewall of the box, have spring constants κ_+ and κ_- , respectively. The box is

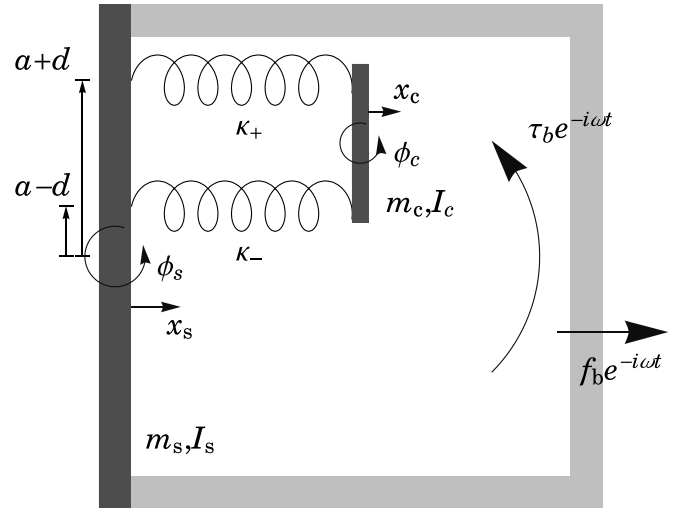


FIG. 2. A rigid shell is coupled to a uniform rod through a pair of massless springs. The mass of the box is evenly distributed on the left sidewall, indicated by the dark shaded region. The translational and rotational oscillations of the rod and the shell are intricately coupled. The resonator experiences an external, time-harmonic external force $f_b e^{-i\omega t}$ and torque $\tau_b e^{-i\omega t}$ about the center of the left sidewall.

harmonically driven by an external force $f_b e^{-i\omega t}$ and external torque $\tau_b e^{-i\omega t}$. The extensions of the upper ϵ_+ and lower ϵ_- springs, for small ϕ_s and ϕ_c , are expressed in terms of the mechanical variables of the box and the rod:

$$\epsilon_{\pm} = -x_s + (a \pm d)\phi_s + x_c \mp d\phi_c. \quad (15)$$

All components oscillate at the driving angular frequency ω in the steady state:

$$-m_s \omega^2 x_s = \kappa_+ \epsilon_+ + \kappa_- \epsilon_- + f_b e^{-i\omega t}, \quad (16a)$$

$$-I_s \omega^2 \phi_s = -\kappa_+ (a+d)\epsilon_+ - \kappa_- (a-d)\epsilon_- + \tau_b e^{-i\omega t}, \quad (16b)$$

$$-m_c \omega^2 x_c = -\kappa_+ \epsilon_+ - \kappa_- \epsilon_-, \quad (16c)$$

$$-I_c \omega^2 \phi_c = \kappa_+ d \epsilon_+ - \kappa_- d \epsilon_-. \quad (16d)$$

Using Eqs. (16c) and (16d), we express the mechanical variables of the core in terms of those of the shell, and eliminate the variables of the core in Eqs. (16a) and (16b) to obtain a generalized form of Newton’s second law:

$$\begin{pmatrix} m_{11}(\omega) & m_{12}(\omega) \\ m_{21}(\omega) & m_{22}(\omega) \end{pmatrix} \begin{pmatrix} \ddot{x}_s \\ \ddot{\phi}_s \end{pmatrix} = \begin{pmatrix} f_b e^{-i\omega t} \\ \tau_b e^{-i\omega t} \end{pmatrix}, \quad (17)$$

where the components of the effective inertia tensor $m_{ij}(\omega)$ are

$$m_{11}(\omega) = m_s + m_c [4\kappa_+ \kappa_- d^2 - I_c (\kappa_+ + \kappa_-) \omega^2] / D(\omega), \quad (18a)$$

$$m_{12}(\omega) = m_{21}(\omega) = -m_c \{4\kappa_+ \kappa_- d^2 a - [\kappa_+ (a+d) + \kappa_- (a-d)] I_c \omega^2\} / D(\omega), \quad (18b)$$

$$m_{22}(\omega) = I_s + \{4\kappa_+ \kappa_- d^2 (I_c + m_c a^2) - [\kappa_+ (a+d)^2 + \kappa_- (a-d)^2] I_c m_c \omega^2\} / D(\omega), \quad (18c)$$

where $D(\omega) \equiv (\kappa_+ + \kappa_- - m_c \omega^2)(\kappa_+ d^2 + \kappa_- d^2 - I_c \omega^2) - (\kappa_+ - \kappa_-)^2 d^2$. The translational or rotational oscillation of the rod excites simultaneously the translational and rotational oscillations of the box. In general, the resonant modes are

superpositions of translation and rotation of the rod. Provided that the two springs are distinct ($\kappa_+ \neq \kappa_-$), the difference in elastic forces in the upper and lower springs introduces nontrivial coupling between translation of the rod and rotation of the box.

In the special case when the springs are identical ($\kappa_+ = \kappa_- = \kappa/2$), the effective inertia tensor of a rod-in-a-box model with identical springs [18] is recovered:

$$m_{11}(\omega) = m_s + \frac{m_c \kappa}{\kappa - m_c \omega^2}, \quad (19a)$$

$$m_{12}(\omega) = m_{21}(\omega) = -\frac{m_c a \kappa}{\kappa - m_c \omega^2}, \quad (19b)$$

$$m_{22}(\omega) = I_s + \frac{I_c \kappa_r}{\kappa_r - I_c \omega^2} + \frac{m_c a^2 \kappa}{\kappa - m_c \omega^2}, \quad (19c)$$

where $\kappa_r = \kappa d^2$ is the torsional spring constant for rotational oscillation. Rotational oscillation of the rod is decoupled from the translation of the box. Nevertheless, the translational oscillation of the rod is coupled to the rotation of the box, if the equilibrium position of the interior rod is off center ($a \neq 0$).

C. Spring tensor

When an object is displaced from the equilibrium in a linear elastic medium, it typically experiences restoring forces

$$\begin{pmatrix} F_x(\mathbf{K}) \\ F_y(\mathbf{K}) \\ F_z(\mathbf{K}) \\ \tau_x(\mathbf{K}) \\ \tau_y(\mathbf{K}) \\ \tau_z(\mathbf{K}) \end{pmatrix} = - \begin{pmatrix} k_{11}(\mathbf{K}) & k_{12}(\mathbf{K}) & k_{13}(\mathbf{K}) & k_{14}(\mathbf{K}) & k_{15}(\mathbf{K}) & k_{16}(\mathbf{K}) \\ k_{21}(\mathbf{K}) & k_{22}(\mathbf{K}) & k_{23}(\mathbf{K}) & k_{24}(\mathbf{K}) & k_{25}(\mathbf{K}) & k_{26}(\mathbf{K}) \\ k_{31}(\mathbf{K}) & k_{32}(\mathbf{K}) & k_{33}(\mathbf{K}) & k_{34}(\mathbf{K}) & k_{35}(\mathbf{K}) & k_{36}(\mathbf{K}) \\ k_{41}(\mathbf{K}) & k_{42}(\mathbf{K}) & k_{43}(\mathbf{K}) & k_{44}(\mathbf{K}) & k_{45}(\mathbf{K}) & k_{46}(\mathbf{K}) \\ k_{51}(\mathbf{K}) & k_{52}(\mathbf{K}) & k_{53}(\mathbf{K}) & k_{54}(\mathbf{K}) & k_{55}(\mathbf{K}) & k_{56}(\mathbf{K}) \\ k_{61}(\mathbf{K}) & k_{62}(\mathbf{K}) & k_{63}(\mathbf{K}) & k_{64}(\mathbf{K}) & k_{65}(\mathbf{K}) & k_{66}(\mathbf{K}) \end{pmatrix} \begin{pmatrix} X \\ Y \\ Z \\ \Phi_x \\ \Phi_y \\ \Phi_z \end{pmatrix}. \quad (20)$$

The wave-vector dependence of the spring tensor can be roughly represented by a nearest-neighbor approximation. For illustration, we consider a lattice of spherical resonator shells of common radii R in a simple cubic lattice of lattice constant a_{sc} . Suppose the resonator centered at the origin displaces from the equilibrium by $X_s \hat{\mathbf{x}}$. By discrete translational symmetry, the resonator centered at $\mathbf{r} = a_{sc} \hat{\mathbf{x}}$ displaces at a phase difference $e^{i\mathbf{K} \cdot \mathbf{r}}$ relative to central resonator. The setup is schematically shown in Fig. 3. The elastic strain $\vec{\epsilon}(\mathbf{r}')$ on

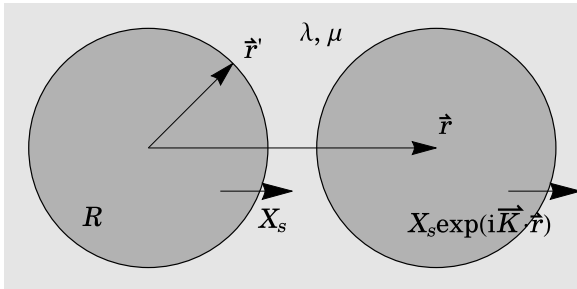


FIG. 3. The elastic strain and stress, and thus the relevant spring tensor component, arise from the relative displacement between resonator shells.

and torques that are proportional to its displacement and the elastic moduli of the background medium. In the same spirit as the generalized Hooke's law, the ij component of the spring tensor k_{ij} describes the generalized force of the i variable, acting on the object, per unit displacement of the j variable. While the spring tensor is conceptually comparable to the stress tensor $\vec{\sigma}$, there are several key distinctions that render the spring tensor an ideal, effective description of phononic crystals. The spring tensor is macroscopically defined, depending on the geometry of the solid inclusions. The components of a spring tensor are adaptable to the relevant degrees of freedom. On the other hand, the stress tensor is microscopically defined, and always has nine components in three dimensions.

In three dimensions, the predominant degrees of freedom of a rigid object are its linear displacement (X, Y, Z) and angular displacement (Φ_x, Φ_y, Φ_z). The associated generalized forces are the force (F_x, F_y, F_z) and the torque (τ_x, τ_y, τ_z) acting on the rigid object by the elastic background. For convenience, we label by the subscripts $i = 1, 2, 3, 4, 5$, and 6 as the directions implied by the generalized coordinates X, Y, Z, Φ_x, Φ_y , and Φ_z respectively. In a three-dimensional phononic crystal consisting of periodic solid embeddings in an elastic background, the Bloch wave vector \mathbf{K} defines the relative separations of the inclusions. The interaction is described by a 6×6 spring tensor:

the surface of the central resonator can be estimated by their relative displacement, per unit distance between the surfaces of the neighboring resonator shell measured on a line parallel to \mathbf{r} :

$$\epsilon_{xx}(\mathbf{r}') \approx \frac{\text{Re}[X_s(e^{i\mathbf{K} \cdot \mathbf{r}} - 1)]}{r - 2R\hat{\mathbf{r}}' \cdot \hat{\mathbf{r}}}. \quad (21)$$

The elastic stress $\vec{\sigma}(\mathbf{r}')$ is linearly proportional to the strain via the constitutive relation (2), specified by Lamé constants λ and μ for the isotropic elastic background. The elastic force \mathbf{F}_b acting on the central resonator, arising from the relative motion with the adjacent resonator, is estimated by an integral of the approximate stress on the surface of the central scatterer:

$$\begin{aligned} \mathbf{F}_b &= \int dS' \vec{\sigma}(\mathbf{r}') \cdot \hat{\mathbf{n}}' \\ &\approx \int_0^{\pi/2} d\theta' 2\pi R^2 \sin \theta' (\lambda + 2\mu) \epsilon_{xx}(\mathbf{r}') \cos \theta' \hat{\mathbf{x}} \\ &= -(2\pi R^2 / b_{NN})(\lambda + 2\mu)[1 - \cos(\mathbf{K} \cdot \mathbf{r})] X_s \hat{\mathbf{x}}, \end{aligned} \quad (22)$$

where $b_{NN} = -2R[1 + (a_{sc}/2R)\ln(1 - 2R/a_{sc})]^{-1}$ ranges from 0 to $2a_{sc}$, depending on the size and separation of the resonators. Similarly analyzed are the elastic forces due to the relative motion between the central resonator and other

nearest neighbors at $\mathbf{r} = -a_{sc}\hat{\mathbf{x}}, \pm a_{sc}\hat{\mathbf{y}}, \pm a_{sc}\hat{\mathbf{z}}$. Ignoring cross interactions, we add up the independent elastic forces to obtain a nearest-neighbor approximation of the spring tensor component $k_{11}(\mathbf{K})$:

$$k_{11}(\mathbf{K}) \equiv -\frac{F_x}{X_s} \approx \frac{4\pi R^2}{b_{NN}} \{(\lambda + 2\mu)[1 - \cos(K_x a_{sc})] + \mu[2 - \cos(K_y a_{sc}) - \cos(K_z a_{sc})]\}. \quad (23)$$

The wave-vector dependence of other spring tensor components can be estimated by symmetry arguments or similar analyses. The simple nearest-neighbor approximation recaptures the wave-vector dependence of the spring tensor (see Fig. 2 in [18]). The actual spring tensor requires a more precise treatment of the elastic strain and interactions with more distant spheres. In subsequent applications, the spring tensor is evaluated numerically by plane wave expansion (in Appendix C) or finite-element method.

D. Acoustic band structure in the EIST model

In the EIST model, the mode spectrum of an acoustic metamaterial is determined by the coupling of resonators in a generic form of Newton's second law:

$$m_{ij}(\omega)\ddot{X}_j = -k_{ij}X_j. \quad (24)$$

The effective inertia $m_{ij}(\omega)$ describes the internal response of an individual resonator. The spring tensor k_{ij} recaptures the coupling of spatially separated resonators in the metamaterial.

In a periodic structure, the spring tensor depends on the underlying lattice symmetry and the wave vector \mathbf{K} . The frequency $f = \omega/(2\pi)$, measured in hertz, is solved at each given \mathbf{K} to yield the acoustic band structure $f(\mathbf{K})$. The theoretically infinite-dimensional eigenvalue problem condenses into a finite-dimensional matrix equation. The eigenfrequencies are the roots of the characteristic equation:

$$\det[k_{ij}(\mathbf{K}) - 4\pi^2 f^2 m_{ij}(f)] = 0. \quad (25)$$

E. Nonresonant scatterers in the EIST model

We demonstrate the efficacy of the EIST model by calculating the acoustic mode spectrum of one of the simplest three-dimensional phononic crystals. It consists of solid cellulose spheres, embedded in a background of open-cell foam, arranged in a simple cubic structure of lattice constant $a_{sc} = 1$ cm. The cellulose spheres occupy $\nu = 50\%$ by volume and have the radius $R = a_{sc}(3\nu/4\pi)^{1/3} \approx 0.4924$ cm. The unit cell is depicted in Fig. 4. Cellulose refers to cellulose nitrate thermoplastics, and is commonly used to make ping-pong balls for its machinability and molding possibilities [54]. The background is an open-cell foam manufactured by Foamex International Inc., containing 0.4-mm pores with 60 pores per inch [55]. Over the acoustic frequency range of interest, the cellulose (foam) is approximated as an isotropic, linear elastic solid with density and Lamé parameters given by $\rho_s = 1350$ kg m⁻³, $\lambda_s = 1.21$ GPa, and $\mu_s = 0.519$ GPa ($\rho = 30$ kg m⁻³, $\lambda = 23.1$ kPa, and $\mu = 15.38$ kPa).

In the EIST framework for an array of rigid, nonresonant balls in soft elastic foam, the predominant degrees of freedom are the translations (X, Y, Z) and rotations (Φ_x, Φ_y, Φ_z) of the

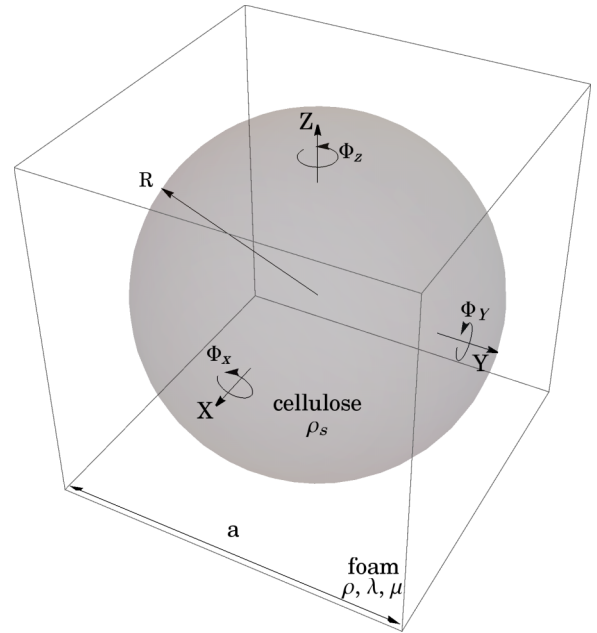


FIG. 4. The unit cell of a nonresonant phononic crystal consists of a cellulose ball of radius $R \approx 0.4924$ cm, surrounded by open-cell foam. The lattice constant is $a_{sc} = 1$ cm. The relevant degrees of freedom are the translation in $x/y/z$ direction $X/Y/Z$, and the rotation $\Phi_x/\Phi_y/\Phi_z$ about the respective coordinate axis.

balls in three orthogonal directions. The effective inertia tensor is diagonal, with the translational inertia and the rotational inertia corresponding to the mass and the moment of inertia, respectively:

$$m_{11} = m_{22} = m_{33} = \frac{4\pi}{3} \rho_s R^3 \approx 0.6750 \text{ g}, \quad (26a)$$

$$m_{44} = m_{55} = m_{66} = \frac{8\pi}{15} \rho_s R^5 \approx 6.546 \text{ g mm}^2. \quad (26b)$$

By Eq. (25), at a given wave vector \mathbf{K} , six eigenfrequencies are solved by diagonalizing the 6×6 matrix eigenvalue equation. When solved throughout the irreducible Brillouin zone, these result in the first six phononic bands, predominated by the coupled translations and rotations in three orthogonal directions of the cellulose balls. The acoustic mode spectrum and the density of states are plotted in Fig. 5. The maximum percentage deviation from the exact finite-element method benchmark is 3.25%. The seventh band, determined by FEM, occurs at over 2800 Hz. The EIST model is physically transparent and computationally efficient in recapturing the first six phononic bands involving the coupled translation and rotation in three orthogonal directions of the cellulose balls. On a mid-range business laptop with a 4-core, double-threaded, central processing unit (CPU) Intel® i7-10510U@4.9GHz, diagonalizing a 6×6 Hermitian matrix in the EIST model takes an average of 10^{-5} s. On the other hand, in the commercial FEM package, about 30 000 degrees of freedom are required to accurately represent the three-dimensional unit cell. On the same laptop, the eigenmode analysis at a given \mathbf{K} point involves a sparse $30\,000 \times 30\,000$ dynamical matrix and takes an average of 10 s.

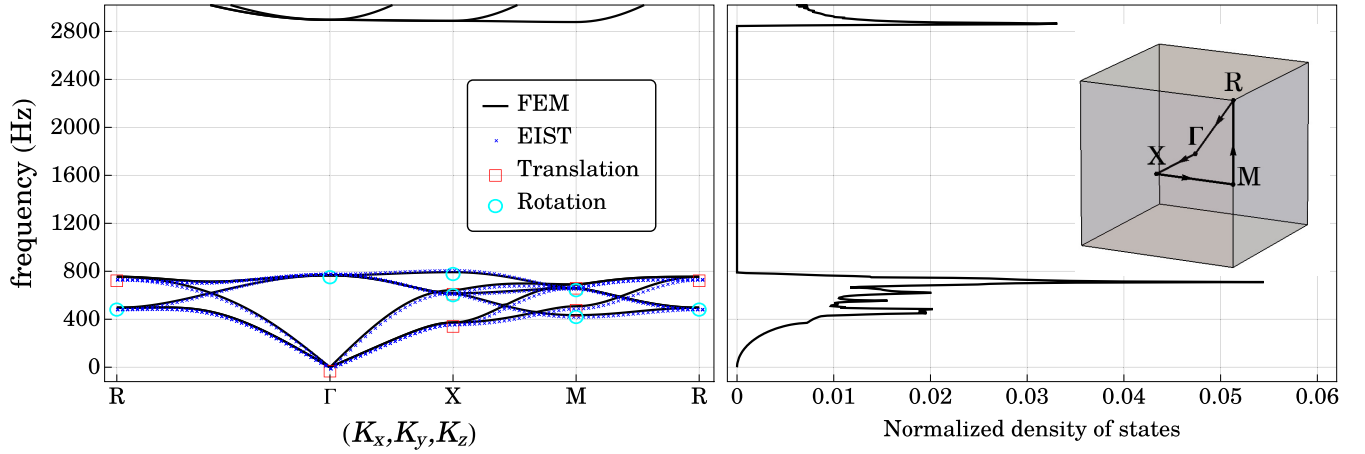


FIG. 5. On the left panel, the acoustic bands of the phonic crystal consisting of a simple cubic lattice of cellulose balls in open-cell foam are plotted in the first Brillouin zone along the path $R \rightarrow \Gamma \rightarrow X \rightarrow M \rightarrow R$. The first six bands involve superposition of rigid body translation and rotation in three orthogonal directions of the cellulose balls, and are recaptured in the EIST model (blue crosses) in Eq. (25). The translational and rotational modes are decoupled at high-symmetry points, indicated by red boxes and cyan circles, respectively. The acoustic bands of the actual phonic crystal are calculated by finite-element method (solid black line). A large Bragg gap occurs approximately in the range from 800 to 2800 Hz. The maximum percentage error of the first six bands is 3.25%. On the right panel, the density of states is evaluated throughout the three-dimensional irreducible Brillouin zone, which is a cube for a simple cubic structure.

The eigenmodes at Γ and R are triply degenerate, with each eigenfrequency corresponding to translation or rotation in three orthogonal directions. At these high-symmetry points, the translational and rotational modes of the cellulose balls are decoupled, and the spring tensor is a diagonal matrix. In general, the translational and rotational oscillations of the cellulose balls are intricately coupled, and the spring tensor is represented by a general, irreducible 6×6 Hermitian matrix. The nontrivial coupling could be appreciated by continuously tracing from the zero-frequency translational mode at Γ (labeled by a red square) to the rotational mode at R (labeled by a cyan circle), and vice versa. Along the path $X \rightarrow M$, the degeneracy is completely lifted, and there are six nondegenerate acoustic bands.

Considerable computational effort is saved by exploiting the lattice symmetry and spherical symmetry of the spherical scatterers. The system is invariant under reflection about the coordinate planes: $f(K_x, K_y, K_z) = f(\pm K_x, \pm K_y, \pm K_z)$, and has fourfold discrete rotational symmetry about the coordinate axes, for example, $f(K_x, K_y, K_z) = f(-K_y, K_x, K_z)$. In other words, the system has the same set of eigenfrequencies, regardless of any coordinate-wise sign reversals and permutations of the Bloch wave vector \mathbf{K} . It suffices to consider a region in the first Brillouin zone, consisting of a triangular pyramid bounded by the planes: $\{0 \leq K_x \leq \pi/a_{sc}, K_x \geq K_y, \text{ and } K_x \leq K_z\}$. The spring tensor and the eigenfrequencies are evaluated at a grid consisting of 1771 independent \mathbf{K} points.

The density of states $\rho_{\text{DOS}}(\omega)$ is formally defined by the number of oscillation modes per unit frequency:

$$\begin{aligned} \rho_{\text{DOS}}(\omega) &= \frac{a_{\text{sc}}^3}{(2\pi)^3} \int d^3\mathbf{K} \delta(\omega - \omega_{\mathbf{K}}) \\ &= \frac{a_{\text{sc}}^3}{(2\pi)^3} \int \frac{d^2\mathbf{K}_{\perp}}{|\nabla_{\mathbf{K}}\omega_{\mathbf{K}}|}, \end{aligned} \quad (27)$$

where $\delta(\omega)$ denotes the Dirac delta function, and $d^2\mathbf{K}_{\perp}$ denotes the \mathbf{K} -space surface area element perpendicular to the gradient of the dispersion relation. In three dimensions, when there is a local extremum or a saddle point in the dispersion relation, the gradient of the dispersion relation vanishes ($\nabla_{\mathbf{K}}\omega_{\mathbf{K}} = \mathbf{0}$). The density of states, which is a \mathbf{K} -space integral over the isofrequency surface, is not divergent but its first derivative is discontinuous. It appears as a kink in the density of states, which is referred to as a Van Hove singularity [56]. The density of states exhibits sharp peaks where the dispersion relation is flat. A prominent peak occurs at 766 Hz, which corresponds to the flat rotational bands at Γ . Moreover, in the zero-frequency limit, the phonic density of states is proportional to the square of the frequency. It is because the dispersion relations are linear near the Brillouin zone center Γ in the static limit, and the density of states scales with the surface area of the spherical isofrequency surface in three dimensions. In numerical computations, a histogram bin width $\Delta\omega$ is specified, and the infinitely sharp delta function is replaced by an appropriate indicator function with a unit area. At a given \mathbf{K} point, if the frequency lies in a histogram bin $n\Delta\omega \leq \omega_{\mathbf{K}} < (n+1)\Delta\omega$, we replace the delta function in Eq. (27) by $[\Theta(\omega - n\Delta\omega) - \Theta(\omega - (n+1)\Delta\omega)]/(\Delta\omega)$, where $\Theta(\omega)$ denotes the Heaviside step function. Here, the density of states histogram is plotted with a frequency bin width of $\Delta f \equiv \Delta\omega/(2\pi) = 5$ Hz, under the normalization condition that the total area under the curve equals the number of acoustic bands. In order to render a smooth density of states profile, the dispersion relations are interpolated to obtain a denser mesh without additional diagonalization and plane wave summation effort.

Calculations of the acoustic spectrum are repeated for an array of cellulose balls in body-centered cubic (bcc) and face-centered cubic (fcc) lattices. To facilitate comparison across different lattice structures, the same radius $R \approx 0.4924$ cm and filling fraction $\nu = 50\%$ are kept. Since there are 2 and 4 spheres per cube in the underlying cubic

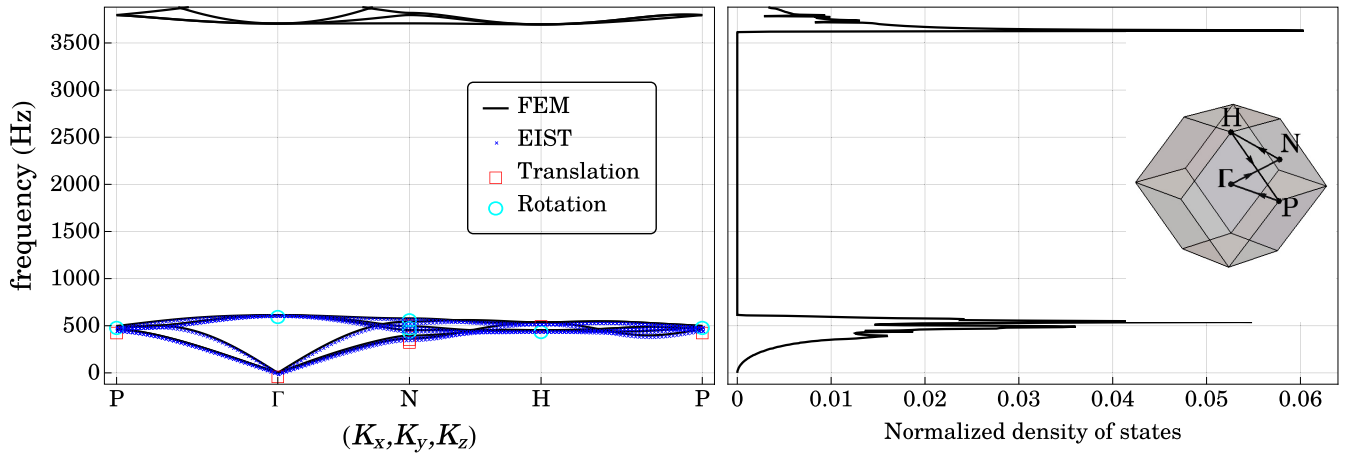


FIG. 6. On the left panel, the acoustic bands of the phononic crystal consisting of a body-centered cubic (bcc) lattice of cellulose balls in open-cell foam are plotted in the first Brillouin zone along the path $P \rightarrow \Gamma \rightarrow N \rightarrow H \rightarrow P$. The first six bands involve superposition of rigid body translation and rotation in three orthogonal directions of the cellulose balls, and are recaptured in the EIST model (blue crosses) in Eq. (25). The translational and rotational modes are decoupled at high-symmetry points, labeled by red boxes and cyan circles, respectively. The acoustic bands of the actual phononic crystal are calculated by finite-element method (solid black line). A large Bragg gap occurs approximately over the frequency range from 600 to 3700 Hz. The maximum percentage error of the first six bands is 1.52%. On the right panel, the density of states is evaluated throughout the three-dimensional irreducible Brillouin zone, which is a rhombic dodecahedron for a bcc structure.

system of bcc and fcc systems, respectively, the lattice spacings are adjusted accordingly to retain the sizes of the balls: $a_{\text{bcc}} = 2^{1/3}a_{\text{sc}} = 2^{1/3}$ cm and $a_{\text{fcc}} = 4^{1/3}a_{\text{sc}} = 2^{2/3}$ cm. The corresponding nearest-neighbor distances are $(\sqrt{3}/2)a_{\text{bcc}} \approx 1.09$ cm for the bcc lattice, and $(\sqrt{2}/2)a_{\text{fcc}} \approx 1.12$ cm for the fcc lattice.

In the EIST representation, the same effective inertia tensor (26a) and (26b) applies to both bcc and fcc systems. The spring tensor, reflecting the interaction among the spherical scatterers, depends on the geometry and lattice structure. In plane wave expansion, the lattice system is characterized by a unique set of reciprocal lattice vectors, over which the plane wave summation is evaluated. Algebraic details are provided in Appendices A and C.

The acoustic mode spectrum and the density of states are plotted in Figs. 6 and 7 for bcc and fcc systems, respectively. Similar techniques involving lattice symmetry and interpolation of the dispersion relation are applied to reduce computational demand and to render smooth density of state profiles. The eigenmodes and the spring tensor are evaluated at a total of 506 (916) independent \mathbf{K} points in the irreducible Brillouin zone of the bcc (fcc) lattice. Over the first six acoustic bands, the maximum percentage deviation from the exact finite-element method benchmark is 1.52% (1.89%) for the bcc (fcc) system, with the next bands occurring at over 3700 Hz (3500 Hz). The accuracy of the EIST model relies on the rigidity of the cellulose balls such that their translations and rotations adequately recapture the low-frequency modes. Our result is consistent with recent topology optimization studies [57] of periodic tungsten carbide and epoxy composites in sc, bcc, and fcc configurations which show that the largest normalized band gaps are achieved in bcc systems.

IV. ANALYTICAL RIGID CORE SHELL APPROXIMATION OF THREE-DIMENSIONAL SPHERICAL RESONATORS

In lattices of local acoustic resonators, dual band gaps can be realized. With suitable parameter choices, both the

Bragg gap and the local resonance gap can be designed to fall within the audible acoustic frequency range. Simple models of locally resonant oscillators typically consist of a dense and stiff core, embedded in an elastically soft medium, encapsulated by a rigid shell. The stiff core and shell are essentially approximated as rigid bodies, as the strain in the stiff core and shell are negligible compared to that of the soft medium. It can be understood from the continuity of the stress tensor across the material boundary and the constitutive equation (2) that, for a fixed stress, the strain is inversely proportional to the stiffness.

On the other hand, the interstitial foam deforms elastically, and the set of elastodynamic equations (5a)–(5c) are necessary to fully recapture its behavior. In the resonators that we study, the core and the shell are orders of magnitude denser than the interstitial medium. Further simplifications can be made, by dropping the mass terms in the elastodynamic equations governing the soft and light interstitial medium. Consequently, the soft and light medium is approximated as a massless elastic material that satisfies elastostatic equilibrium. A relevant dimensionless small parameter is $\epsilon_r = \rho\omega^2 D^2/\mu$, where D denotes the typical thickness of soft and light medium. Using the density of a typical elastic foam $\rho \approx 30$ kg m⁻³, second Lamé parameter $\mu \approx 15$ 000 Pa, and a thickness of $D \approx 1$ mm, we obtain a frequency scale $f_T = (1/2\pi D)\sqrt{\mu/\rho} \approx 3600$ Hz. The elastostatic equilibrium approximation is valid, as long as the frequency in consideration is significantly smaller than f_T . At frequencies near f_T , overtone modes with nodes within the interstitial medium occur, and internal wavelike behavior cannot be ignored.

These assumptions collectively form the basis of the rigid core-shell approximation (RCSA) [17,19]. A simple locally resonant oscillator in three dimensions is spherically symmetric. We consider a dense and stiff spherical core, surrounded by a spherically annular layer of soft elastic foam, encapsulated by a rigid spherical shell. Such resonators exhibit two types of modes: (1) rotational modes involving the relative rotation of the core and the shell, and (2) trans-

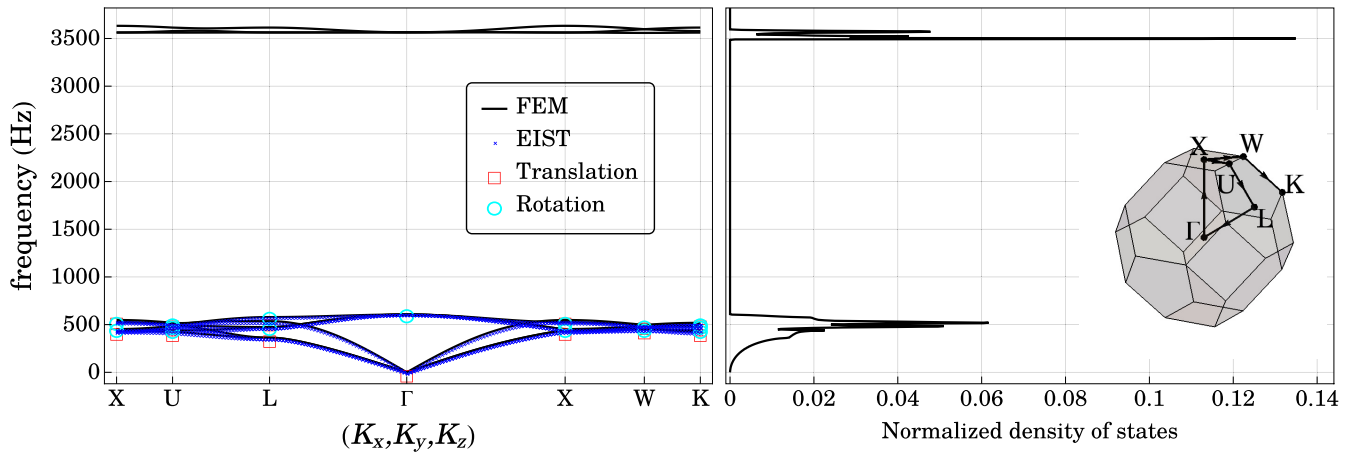


FIG. 7. On the left panel, the acoustic bands of the phononic crystal consisting of a face-centered cubic (fcc) lattice of cellulose balls in open-cell foam are plotted in the first Brillouin zone along the path $X \rightarrow U \rightarrow L \rightarrow \Gamma \rightarrow X \rightarrow W \rightarrow K$. The first six bands involve superposition of rigid body translation and rotation in three orthogonal directions of the cellulose balls, and are recaptured in the EIST model (blue crosses) in Eq. (25). The translational and rotational modes are decoupled at high-symmetry points, labeled by red boxes and cyan circles, respectively. The acoustic bands of the actual phononic crystal are calculated by finite-element method (solid black line). A large Bragg gap occurs approximately over the frequency range from 600 to 3500 Hz. The maximum percentage error of the first six bands is 1.89%. On the right panel, the density of states is evaluated throughout the three-dimensional irreducible Brillouin zone, which is a truncated octahedron for a fcc structure.

lational modes involving their relative translations. Under spherical symmetry, the mechanics in three orthogonal directions are identical, and all the three translational and the three rotational modes are decoupled. The spherically symmetric resonator and the two types of modes are depicted in Fig. 8. We derive closed-form, algebraic expressions for the frequency-dependent, effective mass and moment of inertia for the translational and rotational modes, respectively. In a general three-dimensional resonator, the translational and rotational modes are coupled, and closed-form solutions are not possible. An example is explored in the dumbbell model introduced in Sec. VI. The solution to the boundary value problem of elastostatic equilibrium is unique, provided that the total elastic potential energy in the bounded region is finite [58].

A. Rotational resonance

When the core rotates relative to the shell, the spherically annular layer of interstitial elastic foam provides a restoring torque. By RCSA, we express the torques acting on the core and the shell in terms of the angles of rotation of the rigid bodies and the material parameters of the foam. The calculation hinges on the strain-stress constitutive relation, and the divergence-free property of the stress tensor at elastostatic equilibrium.

Consider a spherical core-shell resonator. The radius of the core is R_1 . The inner and outer radii of the spherical shell are R_2 and R_3 , respectively. The spherically annular region between the core and the shell is filled with a homogeneous, isotropic, linear elastic material of Lamé parameters λ and μ . Suppose the core rotates by the angular displacement $\Phi_c \hat{z}$ and the shell by $\Phi_s \hat{z}$. The directions of rotation are chosen to coincide with the z axis for convenience. The same analysis applies to an arbitrary direction of rotational axis in three dimensions by spherical symmetry and superposition in

linear elasticity. The elastic foam deforms from the equilibrium under a displacement profile $\mathbf{u}(\mathbf{r}) = b(r) \sin \theta \hat{\phi}$, where

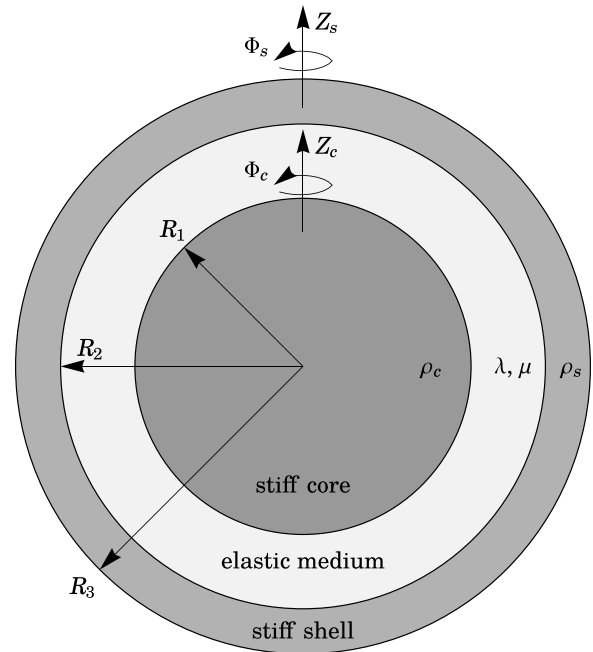


FIG. 8. A spherically symmetric resonator is composed of a stiff and dense spherical core of radius R_1 , surrounded a spherically annular layer of elastic material, enclosed by a stiff spherical shell of inner radius R_2 and outer radius R_3 . By RCSA, the core (shell) is approximated as a rigid body, and the only relevant material parameter is its density ρ_c (ρ_s). In contrast, the elastic material satisfies elastostatic equilibrium, and the relevant material parameters are the Lamé parameters λ and μ . The rigid core (shell) is disturbed from the equilibrium by a linear displacement Z_c (Z_s) and an angular displacement Φ_c (Φ_s).

$b(r)$ is a twice-differentiable function, satisfying the boundary conditions

$$b(R_1) = R_1 \Phi_c, \quad (28a)$$

$$b(R_2) = R_2 \Phi_s. \quad (28b)$$

The detailed elasticity analysis of the rotational modes is provided in Appendix D. The strain and stress tensors are expressed in terms of the displacement field by Eqs. (1) and (2). Then, the divergence-free property of the stress tensor under elastostatic equilibrium is applied to obtain an ordinary differential equation governing the displacement field. The solution $b(r)$ to the boundary value problem, expressible in closed form, is integrated on the inner spherical surface interacting with the core, and the outer surface touching the shell to determine the required torques.

The elasticity calculations in Appendix D result in the elastic restoring torque per unit angular displacement [see Eqs. (D7a) and (D7b)]:

$$\kappa_r = \frac{8\pi\mu R_1^3 R_2^3}{R_2^3 - R_1^3}. \quad (29)$$

The equations of rotational motion of the core and the shell are mapped to a mass-in-a-box model with a massless spring:

$$I_c \ddot{\Phi}_c = \kappa_r (\Phi_s - \Phi_c), \quad (30a)$$

$$I_s \ddot{\Phi}_s = \tau(\omega) + \kappa_r (\Phi_c - \Phi_s), \quad (30b)$$

where $I_c = (8\pi/15)\rho_c R_1^5$ denotes the moment of inertia of the core, $I_s = (8\pi/15)\rho_s (R_3^5 - R_2^5)$ denotes the moment of inertia of the shell, and $\tau(\omega)$ denotes an external, time-harmonic torque acting on the resonator shell at angular frequency ω . By dynamic condensation in Eq. (10b), the frequency-dependent, effective moment of inertia is

$$I_e(f) = I_s \left(\frac{f_{*,r}^2 - f^2}{f_{0,r}^2 - f^2} \right). \quad (31)$$

Here, $f_{0,r}$ and $f_{*,r}$ are the resonant and zero-mass frequencies of the fundamental rotational mode of the resonator:

$$f_{0,r} \equiv \frac{1}{2\pi} \left(\frac{\kappa_r}{I_c} \right)^{1/2}, \quad (32a)$$

$$f_{*,r} \equiv \frac{1}{2\pi} \left(\frac{\kappa_r}{I_c} + \frac{\kappa_r}{I_s} \right)^{1/2}. \quad (32b)$$

B. Translational resonance

We now derive the frequency-dependent, effective mass describing the translational oscillation of the spherical core-shell resonator. The RCSA analysis depends on the rigidity of the core and the shell, as well as the elastostatic equilibrium of the interstitial elastic material.

Suppose the core is displaced from the equilibrium by $Z_c \hat{z}$, and the shell by $Z_s \hat{z}$. The elastic deformation of the interstitial elastic material, and hence the restoring forces, only depend on the relative displacement of the two rigid bodies. By linearity and spherical symmetry, there is no loss of generality when the displacements are chosen in the z direction. The elastic foam deforms from the equilibrium under a displacement profile $\mathbf{u}(\mathbf{r}) = c_r(r) \cos \theta \hat{\mathbf{r}} + c_\theta(r) \sin \theta \hat{\boldsymbol{\theta}}$, where $c_r(r)$

and $c_\theta(r)$ are twice-differentiable functions, satisfying the boundary conditions

$$c_r(R_1) = Z_c, \quad (33a)$$

$$c_r(R_2) = Z_s, \quad (33b)$$

$$c_\theta(R_1) = -Z_c, \quad (33c)$$

$$c_\theta(R_2) = -Z_s. \quad (33d)$$

We summarize the essential physical ideas of the elasticity analysis here, and present the detailed calculations in Appendix E. The strain tensor is expressed in terms of the displacement field by Eq. (1), and so does the stress tensor by the constitutive relation (2). When there is no external body force acting on the idealized, massless, interstitial elastic material, the stress tensor is divergence free, which yields a set of coupled, second-order, linear differential equations governing the displacement profile $\{c_r, c_\theta\}$. The boundary value problem is solved in closed form, and the forces acting on the core and the shell are evaluated by the surface integrals of the stress over the inner and outer spherical surfaces, respectively.

The equations of motion of the core and the shell are mapped to a mass-in-a-box model with a massless spring:

$$m_c \ddot{Z}_c = \kappa_t (Z_s - Z_c), \quad (34a)$$

$$m_s \ddot{Z}_s = f(\omega) + \kappa_t (Z_c - Z_s). \quad (34b)$$

Here, $m_c = (4\pi/3)\rho_c R_1^3$ is the mass of the core. $m_s = (4\pi/3)\rho_s (R_3^3 - R_2^3)$ is the mass of the shell, $f(\omega)$ denotes an external, time-harmonic force acting on the resonator shell in the z direction at angular frequency ω , and κ_t is the elastic spring constant given in Eqs. (E9a) and (E9b) in Appendix E:

$$\begin{aligned} \kappa_t = & \left[24\pi\mu(\lambda + 2\mu)(\lambda + 4\mu)R_1R_2(R_2^5 - R_1^5) \right] / \\ & \left\{ (R_2 - R_1)^2 [\lambda^2(R_2 - R_1)^2(4R_1^2 + 7R_1R_2 + 4R_2^2) \right. \\ & + 2\lambda\mu(13R_1^4 + 8R_1^3R_2 + 3R_1^2R_2^2 + 8R_1R_2^3 + 13R_2^4) \\ & \left. + 5\mu^2(8R_1^4 + 7R_1^3R_2 + 6R_1^2R_2^2 + 7R_1R_2^3 + 8R_2^4)] \right\}. \end{aligned} \quad (35)$$

By dynamic condensation in Eq. (10b), the frequency-dependent, effective mass of the resonator is

$$m_e(f) = m_s \left(\frac{f_{*,t}^2 - f^2}{f_{0,t}^2 - f^2} \right). \quad (36)$$

Here, $f_{0,t}$ and $f_{*,t}$ are the resonant and zero-mass frequencies of the fundamental translational mode of the resonator:

$$f_{0,t} = \frac{1}{2\pi} \left(\frac{\kappa_t}{m_c} \right)^{1/2}, \quad (37a)$$

$$f_{*,t} = \frac{1}{2\pi} \left(\frac{\kappa_t}{m_c} + \frac{\kappa_t}{m_s} \right)^{1/2}. \quad (37b)$$

V. LOCALLY RESONANT PHONONIC CRYSTALS IN THE EIST MODEL

When the solid cellulose spheres in Sec. III E are replaced by local resonators, it is possible to create two large band gaps within the audible acoustic frequency spectrum. In addition to the previously discussed Bragg gap, a large local resonance gap may also appear. This extraordinary dual-band-gap

configuration may enable a broad range of sound sculpting over the audible spectrum. We analyze the acoustic band structure of a lattice of the core-shell resonators introduced in Sec. IV in sc, bcc, and fcc configurations. In the EIST model, the frequency-dependent, effective mass in Eq. (36) and moment of inertia in Eq. (31) constitute the effective inertia tensor of the resonator. On the other hand, interactions among different types of modes of the resonators are recaptured by the wave-vector-dependent spring tensor. The acoustic mode spectrum is governed by a generic form of Newton's second law (24). The results agree within 3.71%, 2.32%, and 2.38% in sc, bcc, and fcc systems, respectively, compared to finite-element method benchmarks. The EIST framework takes into consideration the internal and external couplings of the predominant degrees of freedom and provides a computationally efficient and physically transparent representation of locally resonant phononic crystals.

We specify the materials and the dimensions of the core-shell resonator from Sec. IV. Spherically symmetric resonators are arranged in sc lattice, with lattice constant $a_{sc} = 1$ cm. In each resonator, a dense and stiff steel ball couple to a concentric, spherical cellulose shell through an interstitial layer of open-cell foam. The background is filled by the same type of open-cell foam. The steel core, interstitial foam, and cellulose shell occupy $v_c = 10\%$, $v_f = 20\%$, and $v_s = 20\%$ by volume, respectively. The radius of the steel core $R_1 = a_{sc}[3v_c/(4\pi)]^{1/3} \approx 2.879$ mm. The inner radius of the cellulose shell $R_2 = a_{sc}[3(v_c + v_f)/(4\pi)]^{1/3} \approx 4.153$ mm and its outer radius $R_3 = a_{sc}[3(v_c + v_f + v_s)/(4\pi)]^{1/3} \approx 4.924$ mm. The cross section of the resonator is sketched in Fig. 8. Over the audible frequency range, steel acts as an isotropic, linear elastic solid of density $\rho_c = 7940$ kg m $^{-3}$ and Lamé parameters $\lambda_c = 107.5$ GPa and $\mu_c = 78.15$ GPa [59]. Material parameters of cellulose and open-cell foam are given in Sec. III E.

The steel core and the cellulose shell are orders of magnitude stiffer than the interstitial foam, and behave as rigid bodies. The mass and moment of inertia of the core (shell) are $m_c \approx 0.7940$ g ($m_s \approx 0.2700$ g) and $I_c \approx 2.633$ g mm 2 ($I_s \approx 3.752$ g mm 2), respectively. Denote by $(X_{c/s}, Y_{c/s}, Z_{c/s})$ and $(\Phi_{c/s,x}, \Phi_{c/s,y}, \Phi_{c/s,z})$ the translations and rotations in three orthogonal directions of the core and shell, respectively. By RCSA, the interstitial foam acts as a massless spring of linear spring constant $\kappa_t \approx 3210$ N m $^{-1}$ and torsional spring constant $\kappa_r \approx 0.01384$ N m, given in Eqs. (29) and (35). The shell couples to the elastic background, so that its generalized coordinates $(X_s, Y_s, Z_s, \Phi_{s,x}, \Phi_{s,y}, \Phi_{s,z})$ are chosen as the predominant degrees of freedom in the EIST model. Since the translational or rotational motion of the core only couples to the translation or rotation of the shell in the same direction, the effective inertia tensor is diagonal. The degrees of freedom of the core condenses into frequency-dependent mass (36) and moment of inertia (31) of the resonator:

$$m_{11}(f) = m_{22}(f) = m_{33}(f) = m_s \left(\frac{f_{*,t}^2 - f^2}{f_{0,t}^2 - f^2} \right), \quad (38a)$$

$$m_{44}(f) = m_{55}(f) = m_{66}(f) = I_s \left(\frac{f_{*,r}^2 - f^2}{f_{0,r}^2 - f^2} \right), \quad (38b)$$

where $f_{0,t} \approx 320.0$ Hz, $f_{*,t} \approx 635.3$ Hz, $f_{0,r} \approx 364.9$ Hz, and $f_{*,r} \approx 476.0$ Hz, given in Eqs. (32a), (32b), (37a), and (37b).

The wave-vector-dependent spring tensor describes the coupling of translational and rotational modes of the resonators in a periodic structure. It depends on the lattice system and the material parameters of the background foam, and is insensitive to the interior of the scatterers. Since the spherical resonators occupy 50% by volume, at the same locations as the cellulose balls in the sc lattice with the same lattice spacing, the same spring tensor from Sec. III E applies.

The mode spectrum is calculated by solving a polynomial equation (25) in the square of frequency, as a function of the Bloch wave vector throughout the irreducible Brillouin zone. As in the case of nonresonant cellulose balls, lattice symmetry is utilized to trim repetitive computations, and the dispersion relation is interpolated from a grid of 1771 independent \mathbf{K} points to smoothen the density of states. The band structure and the normalized density of states are plotted in Fig. 9. The maximum deviation from the exact FEM benchmark is 1.79% for the first six bands and 3.71% for the 7th band to the 12th band. The 13th band occurs at over 2800 Hz, involving deformation of the cellulose shell.

The calculations are repeated in bcc and fcc arrangements of the aforementioned core-shell resonators. The lattice spacings are again chosen to retain the filling fraction of 50%, so that $a_{bcc} = 2^{1/3}a_{sc} = 2^{1/3}$ cm and $a_{fcc} = 4^{1/3}a_{sc} = 2^{2/3}$ cm. The resonators are represented by the same frequency-dependent, effective inertia tensor (38a) and (38b) in both the bcc and fcc systems. The spring tensors are inherited from those for the bcc and fcc lattices of cellulose balls in Sec. III E since the resonators occupy the same spaces as the cellulose balls in the corresponding structures.

The acoustic band structure and the normalized density of states are plotted in Figs. 10 and 11, respectively. The eigen-solutions are determined at 506 and 916 independent \mathbf{K} points in the irreducible Brillouin zones of the bcc and fcc structures, respectively. We take advantage of the reflectional and discrete rotational symmetry of the lattice systems to truncate repetitive steps. Assuming the continuity of the eigenfrequencies as a function of the wave vector, we interpolate the dispersion relations to enhance the sampling for the density of states. For the bcc (fcc) system, the maximum percentage deviation of the EIST model predictions from the exact FEM results are 1.62% (2.01%) for the first six bands, and 2.32% (2.38%) for the 7th band to the 12th bands. The 13th band occurs at over 3700 Hz (3500 Hz), which is associated with deformations of the cellulose shell.

There is a complete, acoustic, local-resonance band gap between the sixth and the seventh bands, irrespective of the lattice structures. The band gap occurs from 348 to 620 Hz for the sc lattice, from 337 to 621 Hz for the bcc, and from 336 to 621 Hz for the fcc. It coincides with the frequency range $f_{0,r} < f < f_{*,r}$ over which the effective mass and the effective moment of inertia of the resonator are simultaneously negative. For a negative-definite effective inertia tensor and a positive-definite spring tensor, there is no real solution to the eigenfrequency in Eq. (24). The band-gap formation is explained by the local resonance of the core-shell resonators. In addition, there is complete Bragg gap between the 12th and the 13th bands. The Bragg gap occurs from approximately

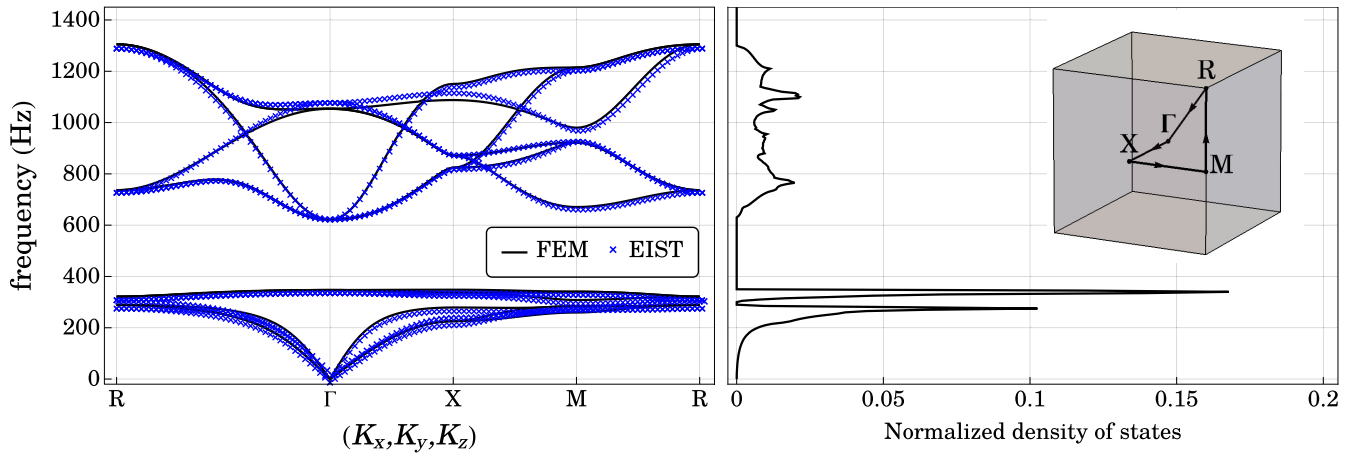


FIG. 9. On the left panel, the first 12 acoustic bands of the phononic crystal consisting of a simple cubic lattice of spherical steel-cellulose resonators in open-cell foam are plotted in the first Brillouin zone along the path $R \rightarrow \Gamma \rightarrow X \rightarrow M \rightarrow R$, for the EIST model (blue crosses) in Eq. (25). The acoustic bands of the actual phononic crystal are calculated by finite-element method (solid black line). The maximum percentage error of the first six bands is 1.79%, and that of the next six bands is 3.71%. On the right panel, the density of states is evaluated throughout the three-dimensional, cubic, irreducible Brillouin zone. There is a complete, local-resonance band gap between 348 to 620 Hz. The Bragg gap spans the frequency range from approximately 1300 to 2800 Hz.

1300 to 2800 Hz for the sc lattice, from approximately 1000 to 3700 Hz for the bcc, and from approximately 1000 Hz to 3500 Hz for the fcc.

There are deep connections between the first 12 acoustic bands and the coupled oscillations of the core and the shell. Over the frequency range of the first three bands, both the effective mass and the moment of inertia are positive, and these bands are closely related to the coupled in-phase translations in three orthogonal directions. On the other hand, over the bulk of the fourth band to the sixth band, the effective mass is negative while the effective moment of inertia is positive. Acoustic modes are heavily influenced by the coupled in-phase rotations in three orthogonal directions. There

are secondary local resonance band gaps between the third band and the fourth band separating the two kinds of acoustic modes, from 289 to 308 Hz for the sc lattice, from 266 to 310 Hz for the bcc, and from 266 to 311 Hz for the fcc. The effective mass and the moment of inertia increase monotonically from the algebraic sum at zero frequency to infinity at the resonant frequency. The six bands for in-phase oscillations are redshifted, compared to a nonresonant solid cellulose sphere described in Sec. III E.

The 7th band to the 12th band are associated with the coupled antiphase translational and rotational vibrations. The effective mass changes its sign at $f = f_{*,t}$, signaling the edges of the degenerate, seventh to ninth bands at Γ , corresponding

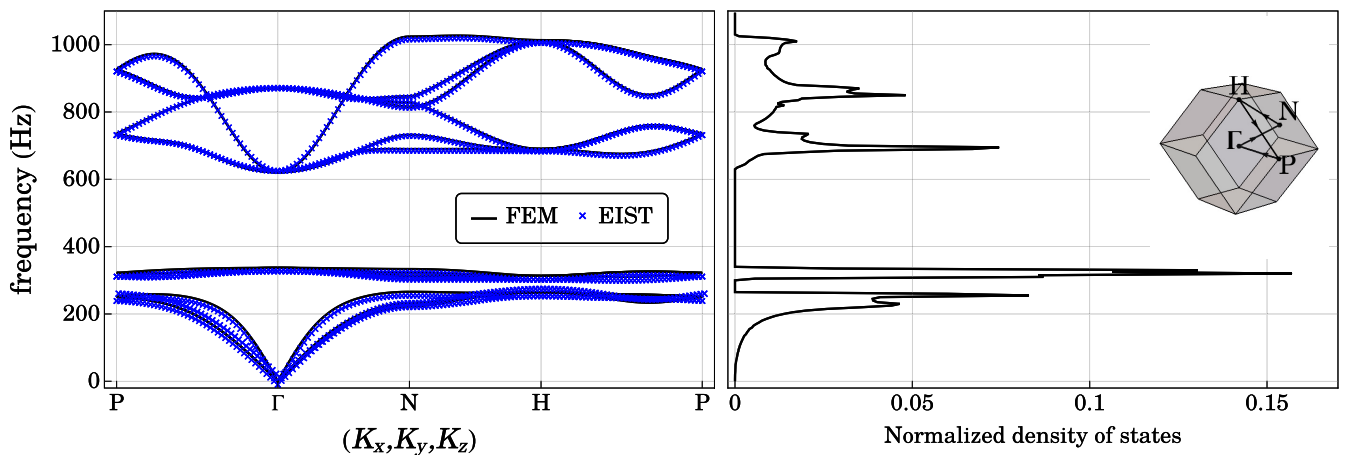


FIG. 10. On the left panel, the first 12 acoustic bands of the phononic crystal consisting of a body-centered cubic (bcc) lattice of spherical steel-cellulose resonators in open-cell foam are plotted in the first Brillouin zone along the path $P \rightarrow \Gamma \rightarrow N \rightarrow H \rightarrow P$, for the EIST model (blue crosses) in Eq. (25). The acoustic bands of the actual phononic crystal are calculated by finite-element method (solid black line). The maximum percentage error of the first six bands is 1.62%, and that of the next six bands is 2.32%. On the right panel, the density of states is evaluated throughout the three-dimensional irreducible Brillouin zone of a rhombic dodecahedron. There is a complete, local-resonance band gap between 337 to 621 Hz. The Bragg gap spans the frequency range from approximately 1000 to 3700 Hz.

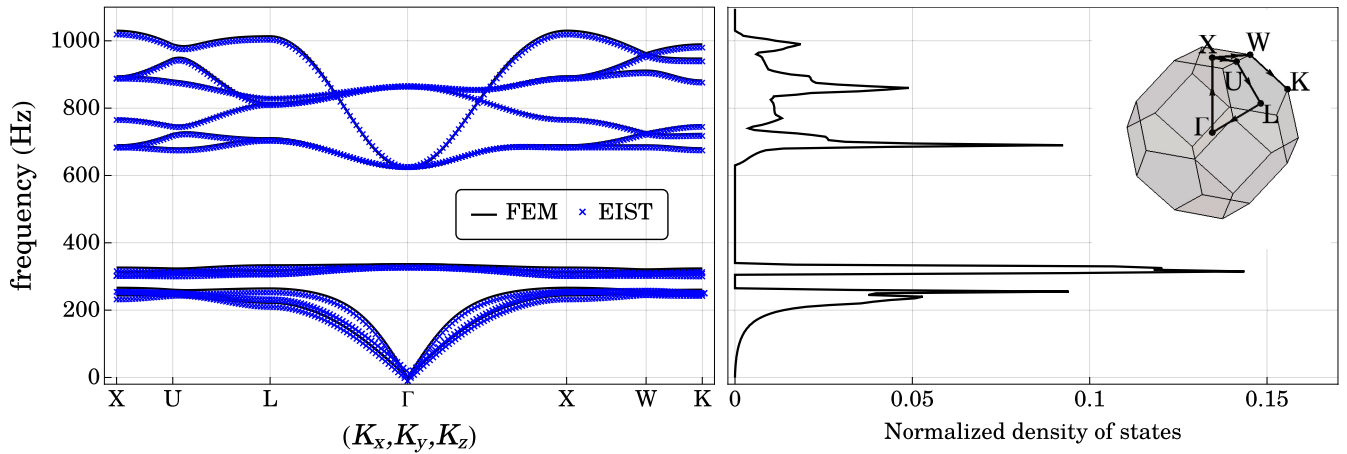


FIG. 11. On the left panel, the first 12 acoustic bands of the phononic crystal consisting of a face-centered cubic (fcc) lattice of spherical steel-cellulose resonators in open-cell foam are plotted in the first Brillouin zone along the path $X \rightarrow U \rightarrow L \rightarrow \Gamma \rightarrow X \rightarrow W \rightarrow K$, for the EIST model (blue crosses) in Eq. (25). The acoustic bands of the actual phononic crystal are calculated by finite-element method (solid black line). The maximum percentage error of the first six bands is 2.01%, and that of the next six bands is 2.38%. On the right panel, the density of states is evaluated throughout the three-dimensional irreducible Brillouin zone of a truncated octahedron. There is a complete, local-resonance band gap between 336 to 621 Hz. The Bragg gap spans the frequency range from approximately 1000 to 3500 Hz.

to the coupled antiphase translational oscillations in three orthogonal directions. Except at the high-symmetry points, the translations and the rotations are intricately coupled. The effective inertia increases monotonically from zero at the zero-mass frequency, and asymptotically approaches that of the resonator shell. Since the effective inertia of the resonator is consistently smaller than that of the nonresonant counterpart of the same static inertia at zero frequency, the six bands for antiphase oscillations are blueshifted.

Potential sources of error of the EIST construction are the massless spring approximation of the interstitial foam and deformations of the cellulose shell. Under the RCSA, the thin layer of interstitial foam is approximated as a massless spring, providing restoring force and torque, when there are relative displacements between the core and the shell. In reality, the foam has a nonzero mass of $m_f = (4\pi/3)\rho_f(R_2^3 - R_1^3)$, and constitutes $m_f/(m_c + m_f + m_s) \approx 0.5607\%$ of the static mass. In addition, a massive spring carries momentum and it takes time for the disturbance to propagate across the layer of foam, so that the forces experienced by the core and the shell do not cancel instantaneously. Analogous arguments apply to the moment of inertia contribution of the foam and the angular momentum propagation across the massive torsional spring. At low frequencies, the translations and rotations in three orthogonal directions of the rigid resonator shell define the predominant degrees of freedom. As the frequency increases, the relative stress across the resonator inevitably excites deformations of the cellulose shell. These effects cause larger percentage deviations of the antiphase bands in comparison to in-phase bands.

VI. ULTRAWIDE LOCAL RESONANCE GAPS AND FLAT ACOUSTIC BANDS

Having applied the EIST model to the spherical core-shell resonators in sc, bcc, and fcc lattices, we extend it to heavier core-shell resonators and dumbbell-shaped resonators. In the

first example, a wide, local-resonance band gap of a dimensionless gap-to-midgap ratio of 126.8% is achieved through increasing the mass difference between the shell and the core. In the next examples, neighboring spherical resonators are joined to create dumbbell-shaped resonators, requiring generalizations to nondiagonal effective inertia tensor and complex Hermitian spring tensor. This enables deterministic engineering of flat acoustic bands within the band gap of the original structure of disconnected spherical resonators. These examples illustrate the simplicity and versatility of the EIST model in describing complex locally resonant oscillators and their interactions in a host medium.

A. Core-shell resonator with wide local-resonance band gap

A wide, local-resonance band gap is achieved, in a lattice of resonators with substantial mass contrasts between the core and the shell. For any given positive-definite spring tensors, there is no real solution to the eigenfrequency whenever the effective inertia tensor is negative-definite. The effective mass of a core-shell resonator is negative between its resonant frequency and zero-mass frequency, and hence the band gap can be extended by simultaneously decreasing the resonant frequency and increasing the zero-mass frequency. By Eq. (11a), the resonant frequency decreases with an increasing mass of the core. On the other hand, by Eq. (11b), the zero-mass frequency increases with a decreasing reduced mass. Analogous arguments apply to the effective moment of inertia governing the rotational modes. By coupling heavy cores to light shells, it is possible to extend the frequency range over which the effective inertia is negative, and correspondingly the band gap.

We illustrate local resonance gap widening using a simple cubic lattice of core-shell resonators developed in Secs. IV and V. To enhance the mass contrast, the filling fractions of steel, interstitial foam, and cellulose are modified to $v_c^{(w)} = 30\%$, $v_f^{(w)} = 10\%$, and $v_s^{(w)} = 10\%$, respectively. The spherically symmetric resonators are arranged in a sc lattice, with

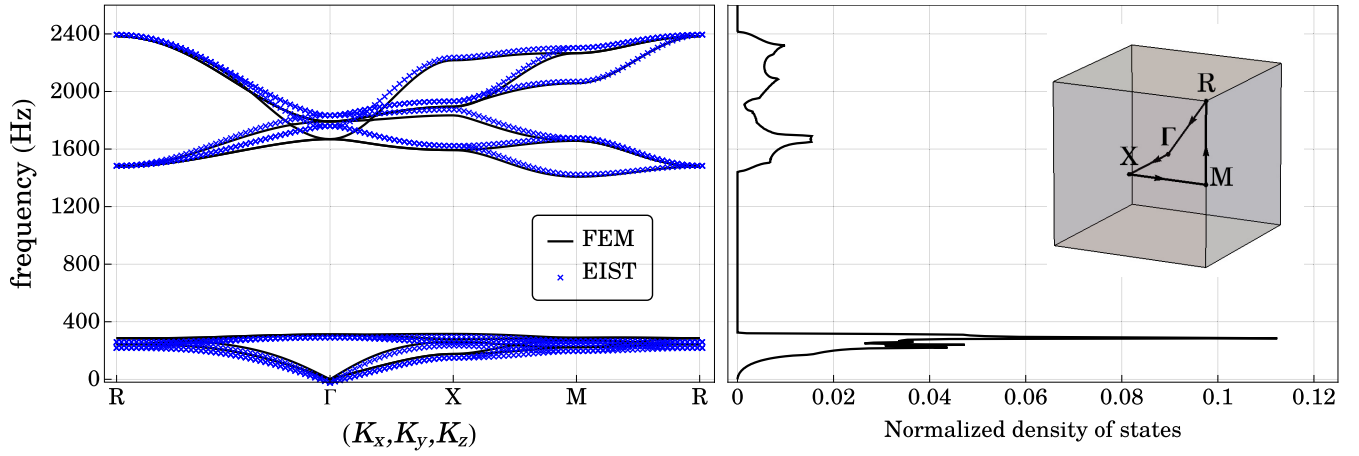


FIG. 12. On the left panel, the first 12 acoustic bands of the phononic crystal consisting of a simple cubic lattice of spherical steel-cellulose resonators of large mass contrast in open-cell foam are plotted in the first Brillouin zone along the path $R \rightarrow \Gamma \rightarrow X \rightarrow M \rightarrow R$, for the EIST model (blue crosses) in Eq. (25). The acoustic bands of the actual phononic crystal are calculated by finite-element method (solid black line). The maximum percentage error of the first six bands is 2.23%, and that of the next six bands is 6.88%. On the right panel, the density of states is evaluated throughout the three-dimensional, cubic, irreducible Brillouin zone. There is a complete, local-resonance band gap between 315.4 to 1408 Hz. The Bragg gap persists over a frequency range from approximately 2400 to 2800 Hz.

lattice constant $a_{sc} = 1$ cm. The radius of the steel core, the inner and outer radii of the cellulose shell are now $R_1^{(w)} = a_{sc}[3v_c^{(w)}/(4\pi)]^{1/3} \approx 4.153$ mm, $R_2^{(w)} = a_{sc}[3(v_c^{(w)} + v_f^{(w)})/(4\pi)]^{1/3} \approx 4.571$ mm, and $R_3^{(w)} = a_{sc}[3(v_c^{(w)} + v_f^{(w)} + v_s^{(w)})/(4\pi)]^{1/3} \approx 4.924$ mm, respectively. The cross section of the resonator is portrayed in Fig. 8. Material parameters of steel, cellulose, and open-cell foam are provided in Secs. III E and V.

The application of the EIST model parallels that in Sec. V. The masses of the resonator are concentrated in the dense and rigid core and the stiff shell. The translations and rotations in three orthogonal directions ($X_{c/s}, Y_{c/s}, Z_{c/s}, \Phi_{c/s,x}, \Phi_{c/s,y}, \Phi_{c/s,z}$) of the core and shell are identified as the principal degrees of freedom. The mass and the moment of inertia of the steel core are triple the previous values: $m_c^{(w)} \approx 2.382$ g and $I_c^{(w)} \approx 16.43$ g mm². In contrast, the mass and the moment of inertia of the shell are roughly halved: $m_s^{(w)} \approx 0.1350$ g and $I_s^{(w)} \approx 2.033$ g mm². The interstitial foam is approximated as a massless spring that couples the steel core and the cellulose shell, with linear spring constant $\kappa_t^{(w)} \approx 16050$ N m⁻¹ and torsional spring constant $\kappa_r^{(w)} \approx 0.1107$ N m, given in Eqs. (29) and (35). Only the resonator shell directly couples to the background material and, hence, in the EIST construction, its generalized coordinates ($X_s, Y_s, Z_s, \Phi_{s,x}, \Phi_{s,y}, \Phi_{s,z}$) are chosen to be the predominant degrees of freedom. The mechanical variables of the core are realized as frequency-dependent terms in the effective mass (36) and moment of inertia (31) of the resonator:

$$m_{11}(f) = m_{22}(f) = m_{33}(f) = m_s^{(w)} \left[\frac{(f_{*,t}^{(w)})^2 - f^2}{(f_{0,t}^{(w)})^2 - f^2} \right], \quad (39a)$$

$$m_{44}(f) = m_{55}(f) = m_{66}(f) = I_s^{(w)} \left[\frac{(f_{*,r}^{(w)})^2 - f^2}{(f_{0,r}^{(w)})^2 - f^2} \right], \quad (39b)$$

where $f_{0,t}^{(w)} \approx 413.2$ Hz, $f_{*,t}^{(w)} \approx 1784.1$ Hz, $f_{0,r}^{(w)} \approx 413.2$ Hz, and $f_{*,r}^{(w)} \approx 1245.2$ Hz, given in Eqs. (32a), (32b), (37a), and (37b). The effective inertia tensor is negative-definite over 413.2 Hz $< f < 1245.2$ Hz, and hence the acoustic band gap based on local resonance must contain such frequency intervals. On the other hand, the same spring tensor from Sec. III E is applicable because the spherical resonators occupy the same positions as the cellulose balls in the lattice and the spring tensor is insensitive to the interior of the scatterers.

The acoustic mode spectrum is determined by solving a degree 12 polynomial equation in the square of frequency, at each given Bloch wave vector in the irreducible Brillouin zone. A smooth density of states is rendered by interpolating the dispersion relations from a mesh of 1771 independent \mathbf{K} -vertex points. The band structure and normalized density of states are plotted in Fig. 12. Compared to the exact FEM benchmark, the maximum percentage deviation is 2.23% for the first six bands, and 6.88% for the 7th to 12th bands. The frequency of the 13th band is over 2800 Hz.

There is a complete, three-dimensional, local-resonance band gap from 315.4 to 1408 Hz. The dimensionless gap-to-mid-gap ratio, defined by the width of the band gap over the central frequency, is 126.8%. Admittedly, the accuracy of the EIST model declines at higher frequencies because the elastostatic equilibrium conditions and the choice of the predominant degrees of freedom do not incorporate the inertial effects of the interstitial foam. Nonetheless, the EIST model provides valuable qualitative insights into the acoustic response of the system. The first (next) six bands are associated with the coupled, in-phase (antiphase) translations and rotations of the core and the shell. The band gap properly contains the frequency range where the effective mass and the effective moment of inertia are simultaneously negative. In other words, the band gap which is based on local resonance can be predicted without detailed information of the spring tensor.

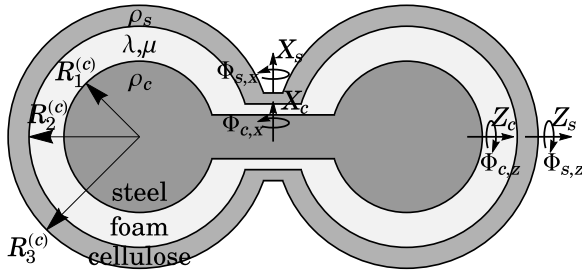


FIG. 13. A conformally coated dumbbell resonator consists of two steel balls of radii $R_1^{(c)} = 2.834$ mm connected via a right circular cylinder of the same material, surrounded by a layer of foam of radii $R_2^{(c)} = 4.140$ mm at the spherical ends, encapsulated by cellulose shell of radii $R_3^{(c)} = 4.924$ mm at the two ends. The radii at the central cylindrical portion of the steel, foam, and cellulose portions are chosen to be $(1/6)R_3^{(c)}$, $(1/4)R_3^{(c)}$, and $(1/3)R_3^{(c)}$, respectively. At low frequencies, the major degrees of freedom are the translation and rotation about the center in three orthogonal directions of the core ($X_c, Y_c, Z_c, \Phi_{c,x}, \Phi_{c,y}, \Phi_{c,z}$), and those of the shell ($X_s, Y_s, Z_s, \Phi_{s,x}, \Phi_{s,y}, \Phi_{s,z}$).

As it is illustrated explicitly, a large, complete, three-dimensional, resonance-based band gap is obtained by coupling heavy cores to light shells. In contrast, tiny band gaps can be designed with small cores and thick shells. It is possible to create a broad spectral range of “localized modes” within the local resonance gap, by introducing a random distribution of core masses and shell thicknesses. A line of identical defects can also serve as a waveguide channel within the local resonance gap.

B. Conformally coated dumbbell resonator

A dumbbell-shaped resonator is created by connecting two neighboring spherical resonators by rigid cylindrical rods. Two steel balls of radius $R_1^{(c)}$, separated by a distance $a^{(c)}$ between their centers, are connected by a cylindrically symmetric steel rod of radius $(1/6)R_3^{(c)}$, where $R_3^{(c)}$ is the outer radius of the spherical shell at either end of the dumbbell. The dumbbell-shaped compound core is conformally coated by a layer of interstitial open-cell foam with inner radius $R_1^{(c)}$ and outer radius $R_2^{(c)}$ at the spherical ends, and inner radius $(1/6)R_3^{(c)}$ and outer radius $(1/4)R_3^{(c)}$ at the cylindrical shaft. The dumbbell-shaped resonator is encapsulated by a stiff cellulose shell of outer radius $R_3^{(c)}$ at the spherical ends and outer radius $(1/3)R_3^{(c)}$ at the cylindrical handle. The direction of azimuthal symmetry is aligned with the z axis. The cross section of the conformally coated dumbbell resonator is depicted in Fig. 13. The conformally coated dumbbell resonators are arranged in a tetragonal lattice with a square base of $a^{(c)} = 1$ cm and height $c^{(c)} = 2a^{(c)} = 2$ cm.

In order to facilitate comparison with the results of the spherical core-shell resonators in Sec. V, the distance between the steel balls is equal to the lattice spacing of the sc lattice $a^{(c)} = 1$ cm, and the filling fractions of steel, cellulose, and open-cell foam in the composite structure are maintained at 10%, 20%, and 70%, respectively. Owing to the additions of the cylindrical connecting rods, the radii of the components are adjusted accordingly: $R_1^{(c)} = 2.834$ mm, $R_2^{(c)} =$

4.140 mm, $R_3^{(c)} = 4.924$ mm. Relevant material parameters of steel, cellulose, and open-cell foam are given in Secs. III E and V. The mass of the dumbbell-shaped core (shell) is $m_c^{(c)} \approx 1.588$ g ($m_s^{(c)} \approx 0.5400$ g). The axial and transversal moments of inertia of the core (shell) are $I_{c,z}^{(c)} \approx 4.886$ g mm² ($I_{s,z}^{(c)} \approx 7.586$ g mm²) and $I_{c,x}^{(c)} = I_{c,y}^{(c)} \approx 42.83$ g mm² ($I_{s,x}^{(c)} = I_{s,y}^{(c)} \approx 21.27$ g mm²), respectively. Detailed calculations are provided in Appendix F.

We apply the EIST model to analyze the acoustic mode spectrum. Over the acoustic frequency range of interest, the mechanical response is dominated by the rigid body translations and rotations about the center of mass in three orthogonal directions of the steel core ($X_c, Y_c, Z_c, \Phi_{c,x}, \Phi_{c,y}, \Phi_{c,z}$) and the cellulose shell ($X_s, Y_s, Z_s, \Phi_{s,x}, \Phi_{s,y}, \Phi_{s,z}$). By azimuthal symmetry and reflectional symmetry, the translation or rotation of the core only couples to the corresponding mechanical variable of the shell in the same direction. The resonator is encapsulated by the dumbbell-shaped shell, such that only the shell couples to the background material. The mechanical responses are mapped to mass-in-a-box models.

We determine the elastic spring constants of the interstitial foam. In the case of the spherical core-shell resonator in Sec. V, an elastostatic equilibrium approximation is applied to the spherically annular layer of interstitial foam to obtain algebraic, closed-form solutions to the spring constants. Similar analytical treatment is unlikely to yield simple, closed-form results in the dumbbell geometry. We resort to FEM to calculate the spring constants for the interior coupling. The elastic force is obtained by integrating the traction vector $\vec{\sigma} \cdot \hat{n}$ of the stationary solution over the boundary of the interstitial foam. The relative displacements of the core and the shell are estimated by averaging the displacement field of the stationary solution in the respective regions. The required spring constants of the fundamental translational resonance are the negative ratios of the elastic forces to the relative displacements: $\kappa_{t,x}^{(c)} = \kappa_{t,y}^{(c)} \approx 7491$ N m⁻¹ and $\kappa_{t,z}^{(c)} \approx 6534$ N m⁻¹. Similar calculations are repeated for the internal, rotational motion to yield the torsional spring constants for the fundamental rotational resonance: $\kappa_{r,x}^{(c)} = \kappa_{r,y}^{(c)} \approx 0.1853$ N m and $\kappa_{r,z}^{(c)} \approx 0.02658$ N m. Compared to the spring constants of the spherical core-shell resonator in Sec. V, the translational spring constants and the axial torsional spring constant are roughly double the corresponding values. On the other hand, the transversal rotational spring constants are an order of magnitude larger. Instead of a simple shear, the transversal rotation also involves compression of the interstitial foam.

The degrees of freedom of the core condense into anisotropic, frequency-dependent masses and moments of inertia of the resonator by Eq. (10b). As the translation or rotation of the core only couples to the corresponding mechanical variable of the shell in the same direction, the resultant effective inertia tensor is diagonal:

$$m_{11}^{(c)}(f) = m_{22}^{(c)}(f) = m_s^{(c)} \left[\frac{(f_{*,l,x}^{(c)})^2 - f^2}{(f_{0,l,x}^{(c)})^2 - f^2} \right], \quad (40a)$$

$$m_{33}^{(c)}(f) = m_s^{(c)} \left[\frac{(f_{*,l,z}^{(c)})^2 - f^2}{(f_{0,l,z}^{(c)})^2 - f^2} \right], \quad (40b)$$

$$m_{44}^{(c)}(f) = m_{55}^{(c)}(f) = I_{s,x}^{(c)} \left[\frac{(f_{*,r,x}^{(c)})^2 - f^2}{(f_{0,r,x}^{(c)})^2 - f^2} \right], \quad (40c)$$

$$m_{66}^{(c)}(f) = I_{s,z}^{(c)} \left[\frac{(f_{*,r,z}^{(c)})^2 - f^2}{(f_{0,r,z}^{(c)})^2 - f^2} \right], \quad (40d)$$

where the resonant and zero-mass frequencies are

$$f_{0,t,x}^{(c)} = \frac{1}{2\pi} \left(\frac{\kappa_{t,x}^{(c)}}{m_c^{(c)}} \right)^{1/2} \approx 345.7 \text{ Hz}, \quad (41a)$$

$$f_{*,t,x}^{(c)} = \frac{1}{2\pi} \left(\frac{\kappa_{t,x}^{(c)}}{m_c^{(c)}} + \frac{\kappa_{t,x}^{(c)}}{m_s^{(c)}} \right)^{1/2} \approx 686.2 \text{ Hz}, \quad (41b)$$

$$f_{0,t,z}^{(c)} = \frac{1}{2\pi} \left(\frac{\kappa_{t,z}^{(c)}}{m_c^{(c)}} \right)^{1/2} \approx 322.8 \text{ Hz}, \quad (41c)$$

$$f_{*,t,z}^{(c)} = \frac{1}{2\pi} \left(\frac{\kappa_{t,z}^{(c)}}{m_c^{(c)}} + \frac{\kappa_{t,z}^{(c)}}{m_s^{(c)}} \right)^{1/2} \approx 640.9 \text{ Hz}, \quad (41d)$$

$$f_{0,r,x}^{(c)} = \frac{1}{2\pi} \left(\frac{\kappa_{r,x}^{(c)}}{I_{c,x}^{(c)}} \right)^{1/2} \approx 331.1 \text{ Hz}, \quad (41e)$$

$$f_{*,r,x}^{(c)} = \frac{1}{2\pi} \left(\frac{\kappa_{r,x}^{(c)}}{I_{c,x}^{(c)}} + \frac{\kappa_{r,x}^{(c)}}{I_{s,x}^{(c)}} \right)^{1/2} \approx 574.8 \text{ Hz}, \quad (41f)$$

$$f_{0,r,z}^{(c)} = \frac{1}{2\pi} \left(\frac{\kappa_{r,z}^{(c)}}{I_{c,z}^{(c)}} \right)^{1/2} \approx 371.3 \text{ Hz}, \quad (41g)$$

$$f_{*,r,z}^{(c)} = \frac{1}{2\pi} \left(\frac{\kappa_{r,z}^{(c)}}{I_{c,z}^{(c)}} + \frac{\kappa_{r,z}^{(c)}}{I_{s,z}^{(c)}} \right)^{1/2} \approx 476.1 \text{ Hz}. \quad (41h)$$

The effective inertia tensor is negative-definite over the frequency range $371.3 \text{ Hz} < f < 476.1 \text{ Hz}$, which must be contained within the acoustic band gap in a lattice of the conformally coated dumbbell resonators.

We calculate the spring tensor describing the coupling between the predominant oscillation modes of a resonator and with those of spatially separated resonators. The spring tensors for spherical scatterers are determined by plane wave expansion in Sec. III E and Appendix C. It is unlikely that a similar plane wave expansion treatment yields a compact lattice sum in the dumbbell geometry. Here, we resort to FEM to calculate the required spring tensor. The elastodynamic equation is solved for the tetragonal lattice where the resonators are replaced by rigid, uniform cellulose dumbbells. Suppose the dumbbell displaces from the equilibrium in the x direction by X_s . The relative displacements of the dumbbells are specified by the Bloch wave vector \mathbf{K} . A generalized elastic force F_j acts on the dumbbell by the background, which can be calculated by integrating over the surface of the scatterer the traction $\vec{\sigma} \cdot \hat{\mathbf{n}}$ and moment $\mathbf{r} \times (\vec{\sigma} \cdot \hat{\mathbf{n}})$. The first column of the spring tensor, associated with translational oscillation in the x direction, is given by $\mathbf{k}_{\text{db},j1}(\mathbf{K}) = -F_j/X_s$. Similar calculations are repeated for other translational and rotational degrees of freedom to calculate the full 6×6 spring tensor.

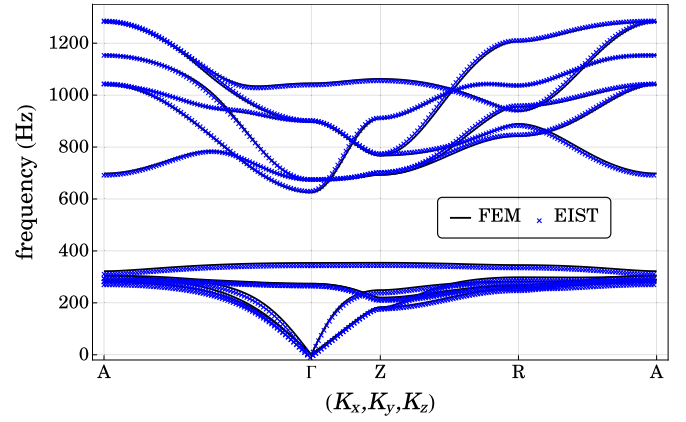


FIG. 14. The first 12 acoustic bands of the phononic crystal consisting of a tetragonal lattice of conformally coated, dumbbell-shaped, steel-cellulose resonators in open-cell foam are plotted along the high-symmetry path $A \rightarrow \Gamma \rightarrow Z \rightarrow R \rightarrow A$ in the irreducible Brillouin zone. The acoustic mode spectrum in the EIST model (blue crosses) is described by a degree 12 polynomial in Eq. (25). The bands of the actual phononic crystal are calculated by finite-element method (black solid line). The maximum percentage error is 3.02%. There is a local resonance band gap from 354.2 to 625.3 Hz. The Bragg gap occurs over a frequency range from approximately 1300 to 2800 Hz.

The acoustic band structure is determined by solving a degree 12 polynomial equation in the square of frequency by Eq. (25). The band diagram is plotted along the high-symmetry path in the irreducible Brillouin zone in Fig. 14. The maximum percentage deviation from the FEM benchmark is 3.02%. The 13th and 14th bands occur at 2800 Hz, involving the c -shaped bending of the steel dumbbell. With a thinner connecting handle, the bending could occur at a lower frequency, and introduce additional mixing with the rigid body translational and rotational motion in the eigenstates. In this study, the translation and rotation in three orthogonal directions of the core and the shell are chosen to be the predominant degrees of freedom, and coupling to other oscillation modes is regarded as sources of error.

There is a complete, local-resonance, acoustic band gap from 354.2 to 625.3 Hz. It properly contains the frequency interval where the effective inertia tensor is negative-definite, confirming the inhibition of wave propagation at negative effective masses and moments of inertia. The width and the frequency range of the acoustic band gap are comparable to those of the spherical core-shell resonators in different lattice configurations. While the mass and axial moments of inertia are doubled through connecting the components of two neighboring units, likewise are the translational and rotational spring constants of the interstitial foam. The characteristic frequencies of the dumbbell resonators, which are related to the ratio of the spring constants to the static inertia, are comparable to those of the original spherical resonators. The band structure of the lattice of dumbbell resonators differs from those of the spherical core-shell resonators in the degrees of degeneracy. At the high-symmetry points in the first Brillouin zone, the triply degenerate translational (rotational) modes split into a nondegenerate axial translational (rotational) mode

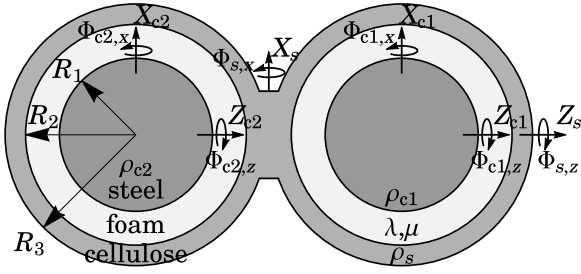


FIG. 15. A conformally coated dumbbell resonator consists of two steel balls of radii $R_1 = 2.879$ mm, individually surrounded by a layer of foam of radius $R_2 = 4.153$ mm, encapsulated by a dumbbell-shaped, cellulose shell of radii $R_3 = 4.924$ mm at the two ends. The radius of the cylindrical handle is $(\frac{1}{3})R_3 \approx 1.641$ mm. At low frequencies, the major degrees of freedom are the translation and rotation about the center of mass in three orthogonal directions of the core on the right ($X_{c1}, Y_{c1}, Z_{c1}, \Phi_{c1,x}, \Phi_{c1,y}, \Phi_{c1,z}$), the core on the left ($X_{c2}, Y_{c2}, Z_{c2}, \Phi_{c2,x}, \Phi_{c2,y}, \Phi_{c2,z}$), and those of the shell ($X_s, Y_s, Z_s, \Phi_{s,x}, \Phi_{s,y}, \Phi_{s,z}$).

in the z direction and doubly degenerate translational (rotational) modes in the x and y directions.

C. Connected shell dumbbell resonator

Another kind of dumbbell-shaped resonator is created by connecting, with a rigid rod, two adjacent spherical, core-shell resonators introduced in Sec. V. Two steel balls of common radii R_1 , separated at a distance $a = 1$ cm, are individually surrounded by a spherically annular layer of open-cell foam of inner radius $R_1 = 2.879$ mm and outer radius $R_2 = 4.153$ mm. The unit is encapsulated by a dumbbell-shaped cellulose shell, consisting of spherical caps of common radii $R_3 = 4.924$ mm at the two ends and a cylindrical handle of radius $(1/3)R_3$. The z axis is chosen to align with the axis of azimuthal symmetry. The cross section of the connected shell dumbbell is depicted in Fig. 15. The dumbbells are arranged in a tetragonal lattice with a square base of $a^{(f)} = 1$ cm and height $c^{(f)} = 2a^{(f)} = 2$ cm, embedded in an elastic background of open-cell foam. Disregarding the differences of the interior of the resonators, the lattice arrangement is identical to conformally coated dumbbell resonators in Sec. VI B. For ease of comparison, we choose the same set of length parameters in Sec. V. Over the audible frequencies, steel, cellulose and open-cell foam are approximated as linear elastic materials. To represent the natural variations of materials in manufacturing, we assume that one of the steel balls is 2% denser: $\rho_{c1} = 7940$ kg m $^{-3}$ and $\rho_{c2} = 1.02\rho_{c1} \approx 8099$ kg m $^{-3}$. This leads to off-diagonal entries in the effective inertia tensor. Other material parameters are provided in Secs. III E and V.

Detailed calculations of the masses and moments of inertia are provided in Appendix F. $m_s^{(f)} \approx 0.5449$ g, $m_{c1}^{(f)} \approx 0.7940$ g, and $m_{c2}^{(f)} = 1.02m_{c1}^{(f)}$ denote the masses of the dumbbell-shaped cellulose shell, the spherical core on the right and the on the left, respectively. $I_{s,z}^{(f)} \approx 7.512$ g mm 2 and $I_{s,x}^{(f)} \approx 21.01$ g mm 2 denote the axial and transversal moments of inertia of the shell, respectively. $I_{c1}^{(f)} \approx 2.633$ g mm 2 and

$I_{c2}^{(f)} = 1.02I_{c1}^{(f)}$ denote the moment of inertia of the two spherical cores.

We analyze the acoustic mode spectrum using the EIST model. Over the frequency range of interest, the primary macroscopic degrees of freedom are the rigid body translations and rotations about center of mass in three orthogonal directions of the shell ($X_s, Y_s, Z_s, \Phi_{s,x}, \Phi_{s,y}, \Phi_{s,z}$), the spherical core on the right ($X_{c1}, Y_{c1}, Z_{c1}, \Phi_{c1,x}, \Phi_{c1,y}, \Phi_{c1,z}$), and the spherical core on the left ($X_{c2}, Y_{c2}, Z_{c2}, \Phi_{c2,x}, \Phi_{c2,y}, \Phi_{c2,z}$).

The spherically annular layer of open-cell foam is approximated as massless spring, such that the linear spring constant $\kappa_t \approx 3210$ N m $^{-1}$ and torsional spring constant $\kappa_r \approx 0.01384$ N m by Eqs. (29) and (35). These values of the spring constant are the same as those of the spherical core-shell resonators in Sec. V because the layers of foam have identical geometries.

By azimuthal symmetry, the translation (axial rotation) in the z direction of the shell only couples to the translations (axial rotations) of the cores in the same direction. Therefore, the translational and rotational oscillations in the axial direction of the dumbbell resonator are mapped to two-masses-in-a-box models. On the other hand, the rotation about the x (y) axis of the shell is not only coupled to the rotations of the cores in the same direction, but also the translations of the cores in the y (x) direction. Hence, the translational and rotational oscillations in the lateral direction are mapped to two-rods-in-a-box model. By Eqs. (19a)–(19c), the nonvanishing components of the effective inertia tensor are

$$m_{33}(f) = m_s^{(f)} + \frac{m_{c1}^{(f)} f_{0,t1}^2}{f_{0,t1}^2 - f^2} + \frac{m_{c2}^{(f)} f_{0,t2}^2}{f_{0,t2}^2 - f^2}, \quad (42a)$$

$$m_{44}(f) = I_{x,s}^{(f)} + \frac{I_{c1}^{(f)} f_{0,r1}^2}{f_{0,r1}^2 - f^2} + \frac{I_{c2}^{(f)} f_{0,r2}^2}{f_{0,r2}^2 - f^2} + \frac{(a^{(f)})^2}{4} \left(\frac{m_{c1}^{(f)} f_{0,t1}^2}{f_{0,t1}^2 - f^2} + \frac{m_{c2}^{(f)} f_{0,t2}^2}{f_{0,t2}^2 - f^2} \right), \quad (42b)$$

$$m_{66}(f) = I_{s,z}^{(f)} + \frac{I_{c1}^{(f)} f_{0,r1}^2}{f_{0,r1}^2 - f^2} + \frac{I_{c2}^{(f)} f_{0,r2}^2}{f_{0,r2}^2 - f^2}, \quad (42c)$$

$$m_{15}(f) = \frac{a^{(f)}(m_{c1}^{(f)} - m_{c2}^{(f)})f_{0,t1}^2 f_{0,t2}^2}{2(f_{0,t1}^2 - f^2)(f_{0,t2}^2 - f^2)}, \quad (42d)$$

where $m_{11}(f) = m_{22}(f) = m_{33}(f)$, $m_{44}(f) = m_{55}(f)$, and $m_{15}(f) = m_{51}(f) = -m_{24}(f) = -m_{42}(f)$. $f_{0,t1} = \sqrt{\kappa_t/m_{c1}^{(f)}}/(2\pi) \approx 320.0$ Hz, $f_{0,t2} = \sqrt{\kappa_t/m_{c2}^{(f)}}/(2\pi) \approx 316.9$ Hz, $f_{0,r1} = \sqrt{\kappa_r/I_{c1}^{(f)}}/(2\pi) \approx 364.9$ Hz, and $f_{0,r2} = \sqrt{\kappa_r/I_{c2}^{(f)}}/(2\pi) \approx 361.3$ Hz are the resonant frequencies of the compound resonator.

The effective mass for axial translational oscillation is schematically plotted in Fig. 16. At zero frequency, the effective mass is the algebraic sum of the masses of the rigid components. The mass of the interstitial layers of foam is ignored in the massless spring approximations. The effective mass increases monotonically from the simple sum at zero frequency to infinity at the first resonant frequency. The shell and the two cores oscillate in phase over the frequency range

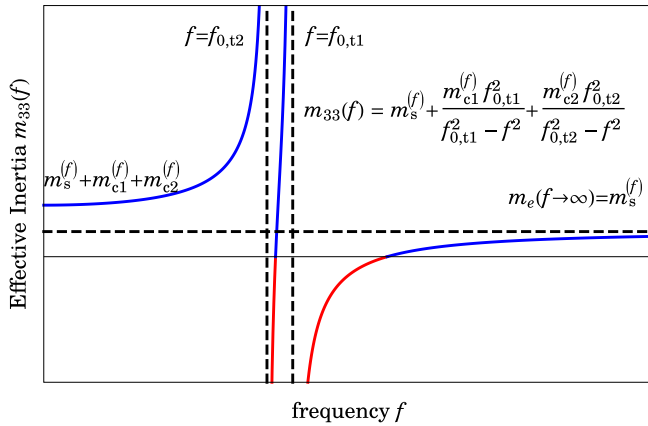


FIG. 16. The frequency-dependent, effective mass (42a) for axial translational oscillation of the dumbbell-shaped, connected shell compound resonator is sketched. There are three positive branches of the effective mass, indicated in blue, with each generating an acoustic band in the EIST model. Provided that the two resonant frequencies are close, it is possible to deterministically engineer a flat acoustic band over the frequency range of the second positive branch. Wave propagation in the given mode is inhibited when the effective mass is negative, indicated in red.

of the first branch. The second branch of positive effective mass lies between the two resonant frequencies. It is possible to engineer flat pass bands, with two local resonances close in resonant frequencies. The shell oscillates in phase with the heavier core ($f < f_{0,t1}$) but antiphase with the lighter core ($f > f_{0,t2}$). The third branch of positive effective mass occurs beyond the second resonant frequency. The effective mass increases monotonically and asymptotically approaches the mass of the shell in the high-frequency limit. The shell oscillates in antiphase with both cores over the frequency range of the third branch.

The same spring tensor in Sec. VIB applies because the dumbbell-shaped resonators occupy the same region as the conformally coated dumbbell resonators. Equipped with the effective inertia and spring tensors, we determine the acoustic band structure by solving a degree 18 polynomial equation in the square of frequency by Eq. (25). The band diagram is plotted along the high-symmetry path in the irreducible Brillouin zone in Figure 17. The 19th and 20th bands occur beyond 2800 Hz, involving c-shaped bending of the dumbbell-shaped cellulose shell. There is a primary local resonance band gap from 363.1 to 618.0 Hz, and a secondary gap from 286.4 to 314.7 Hz. The frequency ranges of the band gaps are consistent with the spherical core-shell resonators in the sc lattice in Fig. 9. Over the frequency range of the 13th band to the 18th band, the shell oscillates in antiphase with both cores. These antiphase bands resemble the 7th to 12th bands of the tetragonal lattice of conformally coated dumbbell resonators in Fig. 14. It is because, in the high-frequency limit, the effective inertia tensor components approach the mass and the moments of inertia of the shell. The same set of spring tensors applies to both kinds of dumbbell resonators, and the masses and moments of inertia of the dumbbell-shaped shells are comparable.

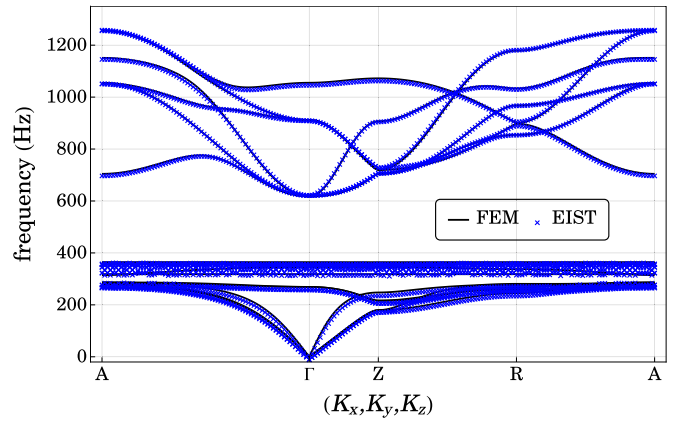


FIG. 17. The first 18 acoustic bands of the phononic crystal consisting of a tetragonal lattice of connected shell, dumbbell-shaped, steel-cellulose resonators in open-cell foam are plotted along the high-symmetry path $A \rightarrow \Gamma \rightarrow Z \rightarrow R \rightarrow A$ in the irreducible Brillouin zone. The acoustic mode spectrum in the EIST model (blue crosses) is described by a degree 18 polynomial in Eq. (25). The bands of the actual phononic crystal are calculated by finite-element method (black solid line). There is a primary local resonance acoustic band gap from 363.1 to 618.0 Hz, and a smaller secondary local resonance gap from 286.4 to 314.7 Hz. A Bragg gap appears over the frequency range from approximately 1300 to 2800 Hz.

A striking feature of the acoustic mode spectrum is the existence of multiple flat bands. In Fig. 18, the band structure is zoomed in over the frequency range 310 to 370 Hz. There is a flat band from 318.1 to 318.2 Hz, within the two frequencies of translational resonance $f_{0,t2} < f < f_{0,t1}$. The shell oscillates in phase with the heavier core and antiphase with the lighter core in the axial direction. More specifically, the two cores oscillate in exactly opposite directions, while the shell, being in phase with the denser core, has a very small oscillation amplitude. It resembles the high-frequency normal modes in the ball-and-stick model of carbon dioxide molecules, where the central carbon atom is stationary and the oxygen atoms vibrate in antiphase. There are two flat bands between 356.9 and 358.7 Hz, and three flat bands between

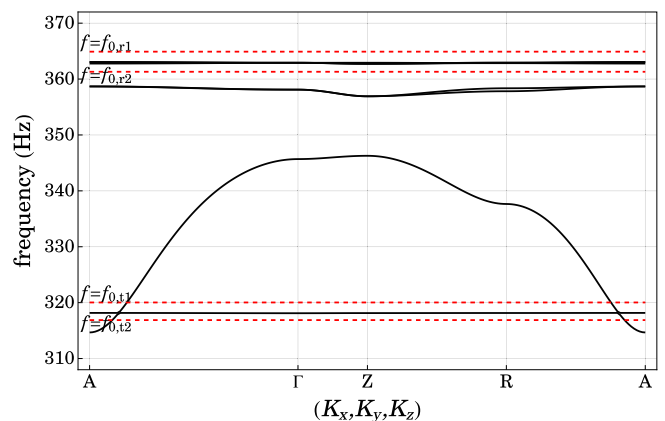


FIG. 18. The acoustic band structure in Fig. 17 is zoomed in over the frequency range 310 to 370 Hz, over which flat acoustic bands occur.

362.7 and 363.1 Hz. The latter flat bands lie within the two frequencies of rotational resonance $f_{0,r2} < f < f_{0,r1}$. Detailed analysis of the off-diagonal terms of the effective inertia tensor is necessary for better understanding of the flat acoustic bands involving intricate coupling of translational and rotational motion. Roughly speaking, when the two interior steel spheres move in antiphase, there is very little net force applied to the dumbbell-shaped cellulose shell that can then propagate to other unit cells of the phononic crystal.

VII. DISCUSSION

In summary, we have identified a variety of phononic crystal architectures, consisting of lattices of local acoustic resonators, which each exhibit a pair of large phononic band gaps in the audible acoustic spectrum. The lower, local resonance band gap is controlled by internal vibrations within each local resonator. The higher Bragg gap is governed by the macroscopic geometrical arrangement of all the individual resonators. The largest local resonance gap is achieved using local resonators with heavy cores and light shells. The largest Bragg gap is achieved using a bcc lattice of local resonators. In the bcc lattice with 50% volume fraction for the local resonators, 50% for the background open-cell foam, and a nearest-neighbor distance of about 1 cm, the bottom of the local resonance gap occurs at about 300 Hz while the top of the Bragg gap occurs at about 3700 Hz. Between these two gaps are a collection of bands that involve antiphase oscillations between the core and the shell of the local resonators. By reducing all the length scales in the phononic crystal by a factor of 2, the frequency scales described above are doubled. Thin layers of two such phononic crystal sheets can be stacked to provide a broad range of sound-blocking material, covering a large part of the audible spectrum. At normal incidence, it is unlikely that an impinging plane wave could effectively couple to the antiphase bands separating the local resonance and Bragg gaps. It would be of considerable interest to explore the coupling to these intervening bands for sound arriving at off-normal incidence.

Our treatment involving a rigid core-shell approximation and the effective inertia spring tensor model provides an intuitive but accurate description of the vibrational modes below the Bragg gap. We have shown that our methodology, likewise, applies to more complex nonspherical local resonators. While we have employed exact numerical methods to evaluate the wave-vector-dependent spring tensor, we have also outlined a simple method for estimating this tensor based on a nearest-neighbor approximation.

In the connected shell dumbbell resonators introduced in Sec. VIC, we are able to deterministically engineer multiple low-frequency, flat acoustic bands between two nearby resonant frequencies. Over the frequency range of the flat bands, the shell oscillates in phase with the heavier core, while the two cores oscillate antiphase with significantly larger amplitudes. Efficient light energy harvesting in thin photonic films via slow-group-velocity optical modes is extensively studied in the literature [60–62]. Similar constructions with acoustic resonators could potentially lead to sound-trapping, slow sound modes in locally resonant acoustic metamaterials. A more realistic treatment of the response of our locally resonant

phononic crystal requires viscoelastic damping effects in the foam.

Generalization of strain-stress constitutive relations is necessary to incorporate dissipative effects for the design of acoustic absorbers. Inelastic losses can be represented by nonzero imaginary parts of the dynamic elastic moduli, as in the conventional Maxwell and Kelvin-Voigt models for viscoelastic materials [63]. While both the translational and rotational resonances are necessary for a complete description of low-frequency acoustic bands, the actual interaction between a resonator and the background is heavily constrained by symmetries. For example, for a spherical resonator with its center situated on a plane of reflectional symmetry, its rotational oscillations do not couple with an impinging elastic wave at normal incidence. Future work will focus on sound absorption of resonators in a background of viscoelastic foam.

Another direction of future research involves control and guiding of acoustic waves by locally resonant phononic metamaterials. Wave propagation is evanescent in the frequency interval of the band gaps. In the locally resonant structures studied in this paper, the band gaps can be broadly classified into local resonance gaps and Bragg gaps. The former is lattice independent, associated with a negative-definite effective inertia tensor. Local resonance gaps are explained by the negative effective masses and moments of inertia. The local resonance gap is sensitive to the detailed internal geometry of the resonators. In contrast, the Bragg gap is sensitive to the lattice arrangements. Defect modes in the Bragg gap can be engineered by disordering the lattice. Careful analyses can potentially open the door to precise engineering of localized cavity modes and waveguide states within locally resonant phononic crystals, for frequency-selective transmission of sound through dual phononic band gaps.

ACKNOWLEDGMENTS

This work was supported in part by the Natural Sciences and Engineering Research Council of Canada. K.L.S.Y. acknowledges receipt of Ted Mossman Memorial Graduate Fellowship and Cray Inc. Fellowships in Physics. K.L.S.Y. thanks M. C. Chu and P. K. Leung of the Chinese University of Hong Kong for support during the pandemic.

APPENDIX A: PLANE WAVE EXPANSION IN 3D

We outline the plane wave expansion (PWE) method in solving the eigenvalue equations of acoustic band structure in three dimensions. The discrete periodicity of a lattice structure is identified by a set of reciprocal lattice vectors \mathbf{G} , which forms a plane wave basis for the Fourier expansion of the underlying material parameters:

$$\rho(\mathbf{r}) = \sum_{\mathbf{G}} \rho(\mathbf{G}) \exp(i\mathbf{G} \cdot \mathbf{r}), \quad (\text{A1})$$

$$(1/C_{pqrs})(\mathbf{r}) = \sum_{\mathbf{G}} (1/C_{pqrs})(\mathbf{G}) \exp(i\mathbf{G} \cdot \mathbf{r}). \quad (\text{A2})$$

Here, C_{pqrs} denotes a nonzero element of the stiffness tensor \mathbf{C} , and $1/C_{pqrs}$ is the reciprocal of that element. The Fourier coefficients are given by an integration over the unit cell of

volume V_c :

$$\mathcal{M}(\mathbf{G}) = \frac{1}{V_c} \int d^3\mathbf{r} \mathcal{M}(\mathbf{r}) \exp(-i\mathbf{G} \cdot \mathbf{r}), \quad (\text{A3})$$

where \mathcal{M} denotes a generic mechanical parameter, such as the mass density ρ , and the reciprocal of nonzero stiffness tensor components $1/C_{pqrs}$.

In the cases that we study, each unit cell contains a rigid sphere of radius R , occupying a filling fraction ν :

$$\nu = \begin{cases} 4\pi R^3 / (3a_{\text{sc}}^3) & \text{for simple cubic lattice,} \\ 8\pi R^3 / (3a_{\text{bcc}}^3) & \text{for body-centered cubic lattice,} \\ 16\pi R^3 / (3a_{\text{fcc}}^3) & \text{for face-centered cubic lattice.} \end{cases} \quad (\text{A4})$$

At a fixed size of the spherical inclusions and a common filling fraction, we choose $a_{\text{bcc}} = 2^{1/3}a_{\text{sc}}$ and $a_{\text{fcc}} = 4^{1/3}a_{\text{sc}}$ to ensure comparability of the results across the lattice structures. When the spherical scatterer is composed of a homogeneous medium, all material parameters are uniform in the interior of the scatterer $r < R$. The Fourier components assume the form

$$\mathcal{M}(\mathbf{G}) = \begin{cases} \mathcal{M}_a \nu + \mathcal{M}_b (1 - \nu) & \text{for } \mathbf{G} = 0, \\ (\mathcal{M}_a - \mathcal{M}_b) 3\nu j_1(GR)/(GR) & \text{for } \mathbf{G} \neq 0. \end{cases} \quad (\text{A5})$$

Here, \mathcal{M}_a is the value of the parameter in the sphere when $r < R$, and \mathcal{M}_b is the value in the background when $r > R$. j_n is the spherical Bessel function of the first kind of order n .

The strain tensor $\vec{\epsilon}$ and the stiffness tensor \mathbf{C} contain a pair of complementary jump discontinuities, in such a way that the product, stress tensor $\vec{\sigma}$, is continuous across any material

boundaries. To ensure numerical convergence, Fourier series with complementary jump discontinuities are multiplied using the inverse rule [22–24]

$$\sum_{\mathbf{G}} \left\{ \sum_{\mathbf{G}'} \left[\frac{1}{C_{pqrs}} \right]^{-1} (\mathbf{G}, \mathbf{G}') \epsilon_{rs}(\mathbf{G}') \right\} \exp(i\mathbf{G} \cdot \mathbf{r}) \rightarrow \sigma_{pq}(\mathbf{r}), \quad (\text{A6})$$

where the matrix denoted by $[1/C_{pqrs}]$ has matrix elements given by $[1/C_{pqrs}](\mathbf{G}, \mathbf{G}') = (1/C_{pqrs})(\mathbf{G} - \mathbf{G}')$. The superscript $^{-1}$ denotes matrix inversion of a nonsingular matrix.

In our three-dimensional elastic composite consisting of linear isotropic materials, the relevant nonvanishing components are $C_{iiii} = \lambda + 2\mu$, $C_{ijij} = \lambda$, and $C_{ijji} = 2\mu$, for $i \neq j$. For notational convenience, we introduce the matrices \mathbf{N}^{inv} , $\mathbf{\Lambda}^{\text{inv}}$, and \mathbf{M}^{inv} , with their elements, respectively, defined by

$$\mathbf{N}_{\mathbf{G}, \mathbf{G}'}^{\text{inv}} = \left[\frac{1}{C_{1111}} \right]^{-1} (\mathbf{G}, \mathbf{G}'), \quad (\text{A7a})$$

$$\mathbf{\Lambda}_{\mathbf{G}, \mathbf{G}'}^{\text{inv}} = \left[\frac{1}{C_{1122}} \right]^{-1} (\mathbf{G}, \mathbf{G}'), \quad (\text{A7b})$$

$$\mathbf{M}_{\mathbf{G}, \mathbf{G}'}^{\text{inv}} = \frac{1}{2} \left[\frac{1}{C_{1212}} \right]^{-1} (\mathbf{G}, \mathbf{G}'). \quad (\text{A7c})$$

We substitute the Bloch wave expansion of the displacement field (6) into the dynamical equations (5a)–(5c). Manipulating the product of the stiffness tensor and the strain tensor elements by the preceding inverse rule (A6) and invoking the orthogonality of the plane wave basis, we obtain an eigenvalue equation governing the acoustic band structure:

$$\sum_{\mathbf{G}'} \left[\begin{pmatrix} D_{11}(\mathbf{G}, \mathbf{G}') & D_{12}(\mathbf{G}, \mathbf{G}') & D_{13}(\mathbf{G}, \mathbf{G}') \\ D_{21}(\mathbf{G}, \mathbf{G}') & D_{22}(\mathbf{G}, \mathbf{G}') & D_{23}(\mathbf{G}, \mathbf{G}') \\ D_{31}(\mathbf{G}, \mathbf{G}') & D_{32}(\mathbf{G}, \mathbf{G}') & D_{33}(\mathbf{G}, \mathbf{G}') \end{pmatrix} - \rho(\mathbf{G} - \mathbf{G}') \omega_{\mathbf{K}}^2 \begin{pmatrix} 1 & 0 & 0 \\ 0 & 1 & 0 \\ 0 & 0 & 1 \end{pmatrix} \right] \begin{pmatrix} \mathbf{u}_{x, \mathbf{K}}(\mathbf{G}') \\ \mathbf{u}_{y, \mathbf{K}}(\mathbf{G}') \\ \mathbf{u}_{z, \mathbf{K}}(\mathbf{G}') \end{pmatrix} = \begin{pmatrix} 0 \\ 0 \\ 0 \end{pmatrix}, \quad (\text{A8})$$

where the elements of the dynamical matrix $\mathbf{D}(\mathbf{G}, \mathbf{G}')$ are

$$D_{11}(\mathbf{G}, \mathbf{G}') = N_{\mathbf{G}, \mathbf{G}'}^{\text{inv}} (K_x + G_x)(K_x + G'_x) + M_{\mathbf{G}, \mathbf{G}'}^{\text{inv}} [(K_y + G_y)(K_y + G'_y) + (K_z + G_z)(K_z + G'_z)], \quad (\text{A9a})$$

$$D_{12}(\mathbf{G}, \mathbf{G}') = \Lambda_{\mathbf{G}, \mathbf{G}'}^{\text{inv}} (K_x + G_x)(K_y + G'_y) + M_{\mathbf{G}, \mathbf{G}'}^{\text{inv}} (K_y + G_y)(K_x + G'_x), \quad (\text{A9b})$$

$$D_{13}(\mathbf{G}, \mathbf{G}') = \Lambda_{\mathbf{G}, \mathbf{G}'}^{\text{inv}} (K_x + G_x)(K_z + G'_z) + M_{\mathbf{G}, \mathbf{G}'}^{\text{inv}} (K_z + G_z)(K_x + G'_x). \quad (\text{A9c})$$

Other matrix elements follow by cyclic permutation symmetry $x \rightarrow y$, $y \rightarrow z$, $z \rightarrow x$. The eigenvalues $\omega_{\mathbf{K}}$ and eigenvectors $(\mathbf{u}_{x, \mathbf{K}}(\mathbf{G}), \mathbf{u}_{y, \mathbf{K}}(\mathbf{G}), \mathbf{u}_{z, \mathbf{K}}(\mathbf{G}))$ describe the oscillation frequency and the configuration of the periodic structure. A general reciprocal lattice wave vector $\mathbf{G} = n_1 \mathbf{G}_1 + n_2 \mathbf{G}_2 + n_3 \mathbf{G}_3$, where n_1 , n_2 , and n_3 are integers and $\{\mathbf{G}_1, \mathbf{G}_2, \mathbf{G}_3\}$ is a set of primitive reciprocal wave vectors. Under the plane wave truncation $|n_{1/2/3}| \leq N$ with $N = 9$, there are $(2N + 1) = 19$ plane waves per direction. In three dimensions, $(2N + 1)^3 = 6859$ plane waves are incorporated. For each pair of reciprocal lattice vectors $(\mathbf{G}, \mathbf{G}')$, the interaction is given by a 3×3 block-dynamical matrix, $\mathbf{D}(\mathbf{G}, \mathbf{G}')$. The full matrix is $20\,577 \times 20\,577$ in size.

We are mostly interested in the first few modes with the smallest eigenfrequencies. Considerable computational time could be saved using an appropriate iterative eigenvalue solver that selects the eigenmodes with the smallest eigenvalues, without compromising the numerical accuracy. We apply the Lanczos algorithm under the shift-invert mode in the Arnoldi package (ARPACK) [64]. For numerical convergence, the dimension of the underlying Krylov subspace is chosen to be two times the number of accurate eigenvalues desired. Conceptually, in each iteration step, components of the trial vectors are damped out, at a rate that increases exponentially with the eigenfrequency, followed by reorthogonalization of all the trial vectors. After rounds of iteration, contributions

of the high-frequency modes are vanishingly small, and the trial vectors approach the orthogonal eigenvectors of the low-frequency modes.

APPENDIX B: ONE-DIMENSIONAL MASSIVE SPRING

For concreteness, we consider a one-dimensional physical example where the spring is composed of a homogeneous, linear elastic material of length l , density ρ , and Lamé parameters λ and μ . We assume that the elastic spring has a uniform cross section of area A , and the elastic deformation is confined in one direction. By Eq. (5a), the longitudinal displacement $u_x(x)$ satisfies the wave equation

$$\rho\omega^2 u_x + (\lambda + 2\mu) \frac{\partial^2 u_x}{\partial x^2} = 0, \quad (\text{B1})$$

where the boundary conditions are specified by the displacements of the shell and the interior mass: $u_x(0) = x_s$ and $u_x(l) = x_c$. The boundary value problem admits a plane wave solution

$$u_x(x) = \csc(k_1 l) [x_s \sin(k_1 l - k_1 x) + x_c \sin(k_1 x)], \quad (\text{B2})$$

where $c_1 = [(\lambda + 2\mu)/\rho]^{1/2}$ is the longitudinal speed of sound and $k_1 \equiv \omega/c_1$ is the longitudinal wave vector. The force f_s/c acting on the shell/core by the spring is

$$f_s = +(\lambda + 2\mu)A \left. \frac{\partial u_x}{\partial x} \right|_{x=0} = -k_1 A (\lambda + 2\mu) [\cot(k_1 l) x_s - \csc(k_1 l) x_c], \quad (\text{B3a})$$

$$f_c = -(\lambda + 2\mu)A \left. \frac{\partial u_x}{\partial x} \right|_{x=l} = -k_1 A (\lambda + 2\mu) [-\csc(k_1 l) x_s + \cot(k_1 l) x_c], \quad (\text{B3b})$$

where elements of the Hermitian coupling matrix [see Eqs. (7a) and (7b)] are identified:

$$\kappa_{11} = \kappa_{22} = +k_1 A (\lambda + 2\mu) \cot(k_1 l), \quad (\text{B4a})$$

$$\kappa_{12} = \kappa_{21} = -k_1 A (\lambda + 2\mu) \csc(k_1 l). \quad (\text{B4b})$$

The frequency-dependent, effective mass of the resonator is given by Eq. (10a). The resonant frequencies $\omega_{0,n}$ are the zeros of the denominator, where n is a non-negative integer denoting the order of the resonant mode. The resonant frequencies are the roots of the implicit equation $\kappa_{22} - m_c \omega^2 = 0$, or

$$\frac{l\omega_{0,n}}{c_1} \tan\left(\frac{l\omega_{0,n}}{c_1}\right) = \frac{\rho A l}{m_c}. \quad (\text{B5})$$

For any non-negative integers n , on the open interval $n\pi < \xi < (n + 1/2)\pi$, the function $\xi \tan(\xi)$ is continuous and increases monotonically from zero to positive infinity. It implies that there is precisely one resonant frequency in the frequency range $\frac{n\pi c_1}{l} \leq \omega_{0,n} \leq (n + \frac{1}{2})\frac{\pi c_1}{l}$.

At acoustic frequencies, the thickness of the elastic material is often negligible compared to the acoustic wavelength ($k_1 l \ll 1$). The displacement profile is a linear function, satisfying an elastostatic equilibrium condition (Laplace equation), and the elastic material behaves as a massless Hookean

spring:

$$u_x(x) \approx x_s [1 - (x/l)] + x_c (x/l), \quad (\text{B6a})$$

$$\kappa_{11} = \kappa_{22} \approx -\kappa_{12} = -\kappa_{21} \approx \kappa \equiv (\lambda + 2\mu)A/l. \quad (\text{B6b})$$

In the massless spring limit, only the fundamental resonant mode ($n = 0$) is relevant. The implicit equation (B5) simplifies to

$$\omega_{0,n=0}^2 \approx \frac{\rho A c_1^2}{m_c l} = \frac{(\lambda + 2\mu)A}{m_c l} = \frac{\kappa}{m_c}, \quad (\text{B7})$$

which agrees with Eq. (11a). In addition, the determinant of the coupling matrix, indeed, vanishes at zero frequency. The effective mass assumes the simple form in Eq. (10b). The elastostatic equilibrium condition allows efficient computation of the massless spring constants in closed-form algebraic expressions of material elastic constants and length parameters. The technique is referred to as the rigid core-shell approximation (RCSA). Previously, it was applied to a cylindrically annular layer of elastic material in two-dimensional locally resonant oscillators (see Sec. III in [19]). In this paper, it is extended to spherically annular layers of elastic material in three-dimensional resonators in Sec. IV and Appendices D and E. In general, the full Hermitian coupling matrix is necessary to recapture the effects of a massive elastic spring. At higher frequencies, the massive spring carries momentum, so that the forces acting on the box and the interior mass by the spring do not cancel out instantaneously.

It is possible to partially incorporate the inertial effects of the elastic material via the first-order correction in density, without the clutter of the full expression. The Hermitian coupling matrix (B4a) and (B4b) is expanded to the first order in the density of the elastic material $\kappa_{ij} \equiv \kappa(2\delta_{ij} - 1) + \tilde{m}_{ij}\omega^2 + O[\omega^4]$, where the first-order correction terms \tilde{m}_{ij} have the unit of mass

$$\tilde{m}_{11} = \tilde{m}_{22} = -\frac{1}{3}\rho A l, \quad (\text{B8a})$$

$$\tilde{m}_{12} = \tilde{m}_{21} = -\frac{1}{6}\rho A l. \quad (\text{B8b})$$

The frequency-dependent, effective mass (10a) of the resonator is expanded up to the first-order correction in the density of the elastic material:

$$m_e^{(1)}(\omega) \approx \frac{1}{\kappa - (m_c - \tilde{m}_{22})\omega^2} \times \{ \kappa(m_s - \tilde{m}_{11} + m_c - \tilde{m}_{22} - \tilde{m}_{12} - \tilde{m}_{21}) + [\tilde{m}_{12}\tilde{m}_{21} - (m_s - \tilde{m}_{11})(m_c - \tilde{m}_{22})]\omega^2 \} \approx (m_s - \tilde{m}_{11}) \left[\frac{(\omega_*^{(1)})^2 - \omega^2}{(\omega_0^{(1)})^2 - \omega^2} \right], \quad (\text{B9})$$

where $\omega_0^{(1)}$ and $\omega_*^{(1)}$ are characteristic frequencies of the resonator with the leading-order correction in the elastic material density:

$$\omega_0^{(1)} = \left(\frac{\kappa}{m_c - \tilde{m}_{22}} \right)^{1/2}, \quad (\text{B10a})$$

$$\omega_*^{(1)} = \left[\frac{\kappa(m_s - \tilde{m}_{11} + m_c - \tilde{m}_{22} - \tilde{m}_{12} - \tilde{m}_{21})}{(m_c - \tilde{m}_{22})(m_s - \tilde{m}_{11})} \right]^{1/2}. \quad (\text{B10b})$$

While the first-order correction shifts the resonant and zero-mass frequencies of the resonator, the effective mass retains the same algebraic form as the massless spring approximation. The correction terms \tilde{m}_{11} and \tilde{m}_{22} can be interpreted as corrections to the masses of the box and the core, respectively. In particular, the modified effective mass correctly reduces to the static mass of the resonator at zero frequency:

$$\begin{aligned} m_e^{(1)}(\omega = 0) &= m_s - \tilde{m}_{11} + m_c - \tilde{m}_{22} - \tilde{m}_{12} - \tilde{m}_{21} \\ &= m_s + m_c + \rho Al, \end{aligned} \quad (\text{B11})$$

where ρAl is the mass of the elastic material.

APPENDIX C: EVALUATION OF SPRING TENSOR BY PLANE WAVE EXPANSION IN 3D

An efficient description of acoustic materials is facilitated by the choice of a set of predominant, macroscopic degrees of freedom, over the desirable range of frequency. When stiff solids are embedded in a soft background, translations (X, Y, Z) and rotations (Φ_x, Φ_y, Φ_z) in three orthogonal directions constitute an effective set of mechanical variables. The associated generalized forces are the force (F_x, F_y, F_z) and the torque (τ_x, τ_y, τ_z) acting on the solid by the elastic back-

ground. The spring tensor k_{ij} is a linear map that relates the mechanical variables and the generalized forces. It describes the coupling of these variables across spatially separated scatterers, with the relative displacements specified by the Bloch wave vector \mathbf{K} in a periodic structure. In this Appendix, we provide the evaluation of the spring tensor by plane wave expansion (PWE). This provides a more exact treatment of the spring tensor, including the elastic forces applied on a given resonator by the background, due to the relative motion with other resonators in the phononic crystals.

Similar to the displacement field (6), the stress tensor can be decomposed into Bloch waves:

$$\sigma_{pq}(\mathbf{r}, t) = \exp(i\mathbf{K} \cdot \mathbf{r} - i\omega_{\mathbf{K}}t) \sum_{\mathbf{G}} \sigma_{pq, \mathbf{K}}(\mathbf{G}) \exp(i\mathbf{G} \cdot \mathbf{r}), \quad (\text{C1})$$

where $\sigma_{pq, \mathbf{K}}(\mathbf{G})$ denotes the Fourier coefficient of the periodic function associated with the pq component of the stress tensor at wave vector \mathbf{K} in the periodic structure. Substituting the displacement field (6) into the linearized strain equation (1) and the constitutive relation (2), we obtain the relevant Fourier components of the stress tensor:

$$\sigma_{xx}(\mathbf{G}) = \sum_{\mathbf{G}'} N_{\mathbf{G}, \mathbf{G}'}^{\text{inv}} u_{x, \mathbf{K}}(\mathbf{G}') (iK_x + iG'_x) + \Lambda_{\mathbf{G}, \mathbf{G}'}^{\text{inv}} [u_{y, \mathbf{K}}(\mathbf{G}') (iK_y + iG'_y) + u_{z, \mathbf{K}}(\mathbf{G}') (iK_z + iG'_z)], \quad (\text{C2a})$$

$$\sigma_{xy}(\mathbf{G}) = \sigma_{yx}(\mathbf{G}) = \sum_{\mathbf{G}'} M_{\mathbf{G}, \mathbf{G}'}^{\text{inv}} [u_{x, \mathbf{K}}(\mathbf{G}') (iK_y + iG'_y) + u_{y, \mathbf{K}}(\mathbf{G}') (iK_x + iG'_x)], \quad (\text{C2b})$$

$$\sigma_{zx}(\mathbf{G}) = \sigma_{xz}(\mathbf{G}) = \sum_{\mathbf{G}'} M_{\mathbf{G}, \mathbf{G}'}^{\text{inv}} [u_{x, \mathbf{K}}(\mathbf{G}') (iK_z + iG'_z) + u_{z, \mathbf{K}}(\mathbf{G}') (iK_x + iG'_x)]. \quad (\text{C2c})$$

Other components follow by cyclic permutation $x \rightarrow y, y \rightarrow z, z \rightarrow x$. Here, the matrices N^{inv} , Λ^{inv} , and M^{inv} are defined in Eqs. (A7a)–(A7c).

The elastic restoring forces acting on the solid due to the background are calculated by integrating the traction $\vec{\sigma} \cdot \hat{\mathbf{n}}$ over the spherical surface of the scatterer. For $i = x/y/z$,

$$\begin{aligned} F_i(\mathbf{K}) &= \oint_{\{r=R\}} dS (\sigma_{ix} \sin \theta \cos \phi + \sigma_{iy} \sin \theta \sin \phi + \sigma_{iz} \cos \theta) \\ &= 4\pi iR^2 \sum_{\mathbf{G}} [\sigma_{ix}(\mathbf{G})(K_x + G_x) + \sigma_{iy}(\mathbf{G})(K_y + G_y) + \sigma_{iz}(\mathbf{G})(K_z + G_z)] \frac{j_1(|\mathbf{K} + \mathbf{G}|R)}{|\mathbf{K} + \mathbf{G}|} e^{-i\omega_{\mathbf{K}}t}. \end{aligned} \quad (\text{C3})$$

The traction provides a torque about the center of the sphere, which is integrated over the spherical surface of the scatterer to yield the net torque acting on the solid by the background:

$$\begin{aligned} \tau_x(\mathbf{K}) &= \oint_{\{r=R\}} dS \hat{\mathbf{x}} \cdot [\mathbf{r} \times (\vec{\sigma} \cdot \hat{\mathbf{r}})] = -4\pi R^3 \sum_{\mathbf{G}} \{\sigma_{zx}(\mathbf{G})(K_x + G_x)(K_y + G_y) + \sigma_{zy}[(K_y + G_y)^2 - (K_z + G_z)^2] \\ &\quad + [\sigma_{zz}(\mathbf{G}) - \sigma_{yy}(\mathbf{G})](K_y + G_y)(K_z + G_z) - \sigma_{yx}(\mathbf{G})(K_x + G_x)(K_z + G_z)\} \frac{j_2(|\mathbf{K} + \mathbf{G}|R)}{|\mathbf{K} + \mathbf{G}|^2} e^{-i\omega_{\mathbf{K}}t}, \end{aligned} \quad (\text{C4a})$$

$$\begin{aligned} \tau_y(\mathbf{K}) &= \oint_{\{r=R\}} dS \hat{\mathbf{y}} \cdot [\mathbf{r} \times (\vec{\sigma} \cdot \hat{\mathbf{r}})] = -4\pi R^3 \sum_{\mathbf{G}} \{\sigma_{xy}(\mathbf{G})(K_y + G_y)(K_z + G_z) + \sigma_{xz}[(K_z + G_z)^2 - (K_x + G_x)^2] \\ &\quad + [\sigma_{xx}(\mathbf{G}) - \sigma_{zz}(\mathbf{G})](K_x + G_x)(K_z + G_z) - \sigma_{zy}(\mathbf{G})(K_x + G_x)(K_y + G_y)\} \frac{j_2(|\mathbf{K} + \mathbf{G}|R)}{|\mathbf{K} + \mathbf{G}|^2} e^{-i\omega_{\mathbf{K}}t}, \end{aligned} \quad (\text{C4b})$$

$$\begin{aligned} \tau_z(\mathbf{K}) &= \oint_{\{r=R\}} dS \hat{\mathbf{z}} \cdot [\mathbf{r} \times (\vec{\sigma} \cdot \hat{\mathbf{r}})] = -4\pi R^3 \sum_{\mathbf{G}} \{\sigma_{yz}(\mathbf{G})(K_x + G_x)(K_z + G_z) + \sigma_{xy}[(K_x + G_x)^2 - (K_y + G_y)^2] \\ &\quad + [\sigma_{yy}(\mathbf{G}) - \sigma_{xx}(\mathbf{G})](K_x + G_x)(K_y + G_y) - \sigma_{xz}(\mathbf{G})(K_x + G_x)(K_z + G_z)\} \frac{j_2(|\mathbf{K} + \mathbf{G}|R)}{|\mathbf{K} + \mathbf{G}|^2} e^{-i\omega_{\mathbf{K}}t}. \end{aligned} \quad (\text{C4c})$$

The integrals are evaluated with the help of the expansion of a plane wave into a series of spherical waves and the orthonormality of spherical harmonics [65]:

$$e^{i\mathbf{K}\cdot\mathbf{r}} = 4\pi \sum_{l=0}^{\infty} \sum_{m=-l}^{+l} i^l j_l(Kr) Y_{lm}(\hat{\mathbf{K}}) Y_{lm}^*(\hat{\mathbf{r}}), \quad (\text{C5})$$

$$\oint d\Omega Y_{lm}^*(\hat{\mathbf{r}}) Y_{l'm'}(\hat{\mathbf{r}}) = \delta_{ll'} \delta_{mm'}, \quad (\text{C6})$$

where Y_{lm} denotes the spherical harmonics of degree l and order m , and the superscript $*$ denotes complex conjugation.

The linear displacement is taken to be the displacement averaged throughout the sphere, whereas the angular displacement is determined by averaging over the spherical surface:

$$X = \frac{3}{4\pi R^3} \int_{\{r<R\}} d^3\mathbf{r} u_x = \sum_{\mathbf{G}} \frac{3j_1(|\mathbf{K} + \mathbf{G}|R)}{|\mathbf{K} + \mathbf{G}|R} u_{x,\mathbf{K}}(\mathbf{G}) e^{-i\omega_{\mathbf{K}}t}, \quad (\text{C7a})$$

$$Y = \frac{3}{4\pi R^3} \int_{\{r<R\}} d^3\mathbf{r} u_y = \sum_{\mathbf{G}} \frac{3j_1(|\mathbf{K} + \mathbf{G}|R)}{|\mathbf{K} + \mathbf{G}|R} u_{y,\mathbf{K}}(\mathbf{G}) e^{-i\omega_{\mathbf{K}}t}, \quad (\text{C7b})$$

$$Z = \frac{3}{4\pi R^3} \int_{\{r<R\}} d^3\mathbf{r} u_z = \sum_{\mathbf{G}} \frac{3j_1(|\mathbf{K} + \mathbf{G}|R)}{|\mathbf{K} + \mathbf{G}|R} u_{z,\mathbf{K}}(\mathbf{G}) e^{-i\omega_{\mathbf{K}}t}, \quad (\text{C7c})$$

$$\begin{aligned} \Phi_x &= \frac{3}{8\pi R^3} \oint_{\{r=R\}} dS (u_z \sin \theta \sin \phi - u_y \cos \theta) \\ &= \frac{3i}{2R} \sum_{\mathbf{G}} [u_{z,\mathbf{K}}(\mathbf{G})(K_y + G_y) - u_{y,\mathbf{K}}(\mathbf{G})(K_z + G_z)] \frac{j_1(|\mathbf{K} + \mathbf{G}|R)}{|\mathbf{K} + \mathbf{G}|} e^{-i\omega_{\mathbf{K}}t}, \end{aligned} \quad (\text{C7d})$$

$$\begin{aligned} \Phi_y &= \frac{3}{8\pi R^3} \oint_{\{r=R\}} dS (u_x \cos \theta - u_z \sin \theta \cos \phi) \\ &= \frac{3i}{2R} \sum_{\mathbf{G}} [u_{x,\mathbf{K}}(\mathbf{G})(K_z + G_z) - u_{z,\mathbf{K}}(\mathbf{G})(K_x + G_x)] \frac{j_1(|\mathbf{K} + \mathbf{G}|R)}{|\mathbf{K} + \mathbf{G}|} e^{-i\omega_{\mathbf{K}}t}, \end{aligned} \quad (\text{C7e})$$

$$\begin{aligned} \Phi_z &= \frac{3}{8\pi R^3} \oint_{\{r=R\}} dS (u_y \sin \theta \cos \phi - u_x \sin \theta \sin \phi) \\ &= \frac{3i}{2R} \sum_{\mathbf{G}} [u_{y,\mathbf{K}}(\mathbf{G})(K_x + G_x) - u_{x,\mathbf{K}}(\mathbf{G})(K_y + G_y)] \frac{j_1(|\mathbf{K} + \mathbf{G}|R)}{|\mathbf{K} + \mathbf{G}|} e^{-i\omega_{\mathbf{K}}t}. \end{aligned} \quad (\text{C7f})$$

The ij th component of the spring tensor is defined as the restoring force/torque acting on the sphere in the i th direction per unit displacement in the j th direction. The 6×6 spring tensor, $\vec{\mathbf{k}}$ with components k_{ij} , is calculated using Eqs. (C3), (C4c) and (C7a)–(C7f):

$$\vec{\mathbf{k}} = - \begin{pmatrix} F_x^{(1)} & F_x^{(2)} & F_x^{(3)} & F_x^{(4)} & F_x^{(5)} & F_x^{(6)} \\ F_y^{(1)} & F_y^{(2)} & F_y^{(3)} & F_y^{(4)} & F_y^{(5)} & F_y^{(6)} \\ F_z^{(1)} & F_z^{(2)} & F_z^{(3)} & F_z^{(4)} & F_z^{(5)} & F_z^{(6)} \\ \tau_x^{(1)} & \tau_x^{(2)} & \tau_x^{(3)} & \tau_x^{(4)} & \tau_x^{(5)} & \tau_x^{(6)} \\ \tau_y^{(1)} & \tau_y^{(2)} & \tau_y^{(3)} & \tau_y^{(4)} & \tau_y^{(5)} & \tau_y^{(6)} \\ \tau_z^{(1)} & \tau_z^{(2)} & \tau_z^{(3)} & \tau_z^{(4)} & \tau_z^{(5)} & \tau_z^{(6)} \end{pmatrix} \begin{pmatrix} X^{(1)} & X^{(2)} & X^{(3)} & X^{(4)} & X^{(5)} & X^{(6)} \\ Y^{(1)} & Y^{(2)} & Y^{(3)} & Y^{(4)} & Y^{(5)} & Y^{(6)} \\ Z^{(1)} & Z^{(2)} & Z^{(3)} & Z^{(4)} & Z^{(5)} & Z^{(6)} \\ \Phi_x^{(1)} & \Phi_x^{(2)} & \Phi_x^{(3)} & \Phi_x^{(4)} & \Phi_x^{(5)} & \Phi_x^{(6)} \\ \Phi_y^{(1)} & \Phi_y^{(2)} & \Phi_y^{(3)} & \Phi_y^{(4)} & \Phi_y^{(5)} & \Phi_y^{(6)} \\ \Phi_z^{(1)} & \Phi_z^{(2)} & \Phi_z^{(3)} & \Phi_z^{(4)} & \Phi_z^{(5)} & \Phi_z^{(6)} \end{pmatrix}^{-1}. \quad (\text{C8})$$

Accordingly, we introduce the band index superscripts $j = 1, 2, 3, 4, 5, 6$ to indicate the first six low-frequency dispersion relations $\omega_{\mathbf{K}}^{(j)}$ and the corresponding eigenvectors that appear in Eqs. (C2a)–(C2c) and (C7a)–(C7f), associated with the coupled translations and rotations of the spheres. The displacement and forces in Eq. (C8) are likewise labeled with the corresponding superscripts.

APPENDIX D: RCSA OF ROTATIONAL MODES

In a spherical core-shell resonator, when the core rotates relative to the shell, the interstitial material acts as a linear elastic material to provide restoring torques. In this Appendix, we determine such torques in terms of the elastic parameters of the interstitial material, and the angles of rotations of the core and the shell. When the acoustic wavelength is

significantly longer than the typical length scales of the resonator, the interstitial material is regarded as massless and satisfies elastostatic equilibrium conditions.

In spherical coordinates, the nontrivial components of the strain tensor are $\epsilon_{r\phi}$ and $\epsilon_{\phi r}$:

$$\begin{aligned}\epsilon_{r\phi} = \epsilon_{\phi r} &= \frac{1}{2} \left(\frac{1}{r \sin \theta} \frac{\partial u_r}{\partial \phi} + \frac{\partial u_\phi}{\partial r} - \frac{u_\phi}{r} \right) \\ &= \frac{1}{2} \left(\frac{db}{dr} - \frac{b}{r} \right) \sin \theta.\end{aligned}\quad (\text{D1})$$

Here, $b(r)$ is defined in Sec. IV A. Using the generalized Hooke's law (2) for isotropic, linear, elastic solid, we conclude that the only nonvanishing components of the stress tensor $\vec{\sigma}$ are $\sigma_{\phi r}$ and $\sigma_{r\phi}$:

$$\sigma_{\phi r} = \sigma_{r\phi} = \mu \left(\frac{db}{dr} - \frac{b}{r} \right) \sin \theta. \quad (\text{D2})$$

The stress tensor satisfies elastostatic equilibrium condition, in the absence of an external body force:

$$\frac{\partial \sigma_{r\phi}}{\partial r} + \frac{1}{r} \frac{\partial \sigma_{\theta\phi}}{\partial \theta} + \frac{1}{r \sin \theta} \frac{\partial \sigma_{\phi\phi}}{\partial \phi} + \frac{1}{r} (2\sigma_{\theta\phi} \cot \theta + 3\sigma_{r\phi}) = 0. \quad (\text{D3})$$

Substituting Eq. (D2) into (D3), we obtain a second-order, linear, ordinary differential equation governing $b(r)$:

$$\mu \left(\frac{d^2 b}{dr^2} + \frac{2}{r} \frac{db}{dr} - \frac{2}{r^2} b \right) = 0. \quad (\text{D4})$$

We solve Eq. (D4) by a standard power-law ansatz and impose the boundary conditions (28a) and (28b) to obtain

$$b(r) = \frac{R_2^3 \Phi_s - R_1^3 \Phi_c}{R_2^3 - R_1^3} r + \frac{E(\Phi_c - \Phi_s)}{r^2}, \quad (\text{D5})$$

$$\sigma_{r\phi} = \sigma_{\phi r} = \frac{3\mu E}{r^3} (\Phi_s - \Phi_c) \sin \theta, \quad (\text{D6})$$

where $E = R_1^3 R_2^3 / (R_2^3 - R_1^3)$. The torque $\tau_{c/s}$ acting on the core/shell is determined by integrating the stress tensor over the spherical boundary $\{r = R_{1/2}\}$:

$$\begin{aligned}\tau_c &= \oint_{\{r=R_1\}} \mathbf{r} \times (\vec{\sigma} \cdot \hat{\mathbf{n}}) dS = \oint_{\{r=R_1\}} -R_1 \sigma_{\phi r} \hat{\boldsymbol{\theta}} dS \\ &= 8\pi \mu E (\Phi_s - \Phi_c) \hat{\mathbf{z}},\end{aligned}\quad (\text{D7a})$$

$$\begin{aligned}\tau_s &= \oint_{\{r=R_2\}} \mathbf{r} \times (\vec{\sigma} \cdot \hat{\mathbf{n}}) dS = \oint_{\{r=R_2\}} +R_2 \sigma_{\phi r} \hat{\boldsymbol{\theta}} dS \\ &= 8\pi \mu E (\Phi_c - \Phi_s) \hat{\mathbf{z}},\end{aligned}\quad (\text{D7b})$$

where $\hat{\mathbf{n}}$ denotes an inward normal vector directing towards the interstitial region of elastic material on the boundary. Here, we have used the basis vector in spherical coordinate: $\hat{\boldsymbol{\theta}} = \cos \theta \cos \phi \hat{\mathbf{x}} + \cos \theta \sin \phi \hat{\mathbf{y}} - \sin \theta \hat{\mathbf{z}}$. Note that the internal torques cancel out in the elastostatic limit, as required by Newton's third law.

APPENDIX E: RCSA OF TRANSLATIONAL MODES

When the core displaces relative to the shell, the spherically annular layer of interstitial elastic foam provides a restoring force. In this Appendix, we express the forces acting

on the core and the shell in terms of the displacements of the rigid bodies and the material parameters of the foam in the long-wavelength limit. The calculation assumes the constitutive relation between the strain and the stress, which is divergence free at elastostatic equilibrium.

In spherical coordinates, the nonvanishing components of the strain tensor ϵ_{rr} , $\epsilon_{\theta\theta}$, $\epsilon_{\phi\phi}$, $\epsilon_{r\theta}$, and $\epsilon_{\theta r}$ are expressed in terms of the functions $c_r(r)$ and $c_\theta(r)$ defined previously in Sec. IV B:

$$\epsilon_{rr} = \frac{\partial u_r}{\partial r} = \frac{dc_r}{dr} \cos \theta, \quad (\text{E1a})$$

$$\epsilon_{\theta\theta} = \frac{1}{r} \frac{\partial u_\theta}{\partial \theta} + \frac{u_r}{r} = \frac{1}{r} (c_r + c_\theta) \cos \theta, \quad (\text{E1b})$$

$$\begin{aligned}\epsilon_{\phi\phi} &= \frac{1}{r \sin \theta} \left(\frac{\partial u_\phi}{\partial \phi} + u_r \sin \theta + u_\theta \cos \theta \right) \\ &= \frac{1}{r} (c_r + c_\theta) \cos \theta,\end{aligned}\quad (\text{E1c})$$

$$\begin{aligned}\epsilon_{r\theta} = \epsilon_{\theta r} &= \frac{1}{2} \left(\frac{1}{r} \frac{\partial u_r}{\partial \theta} + \frac{\partial u_\theta}{\partial r} - \frac{u_\theta}{r} \right) \\ &= \frac{1}{2} \left[\frac{dc_\theta}{dr} - \frac{1}{r} (c_r + c_\theta) \right] \sin \theta.\end{aligned}\quad (\text{E1d})$$

We use the generalized Hooke's law (2) for isotropic, linear, elastic solid to conclude that the nonvanishing components of the stress tensor are σ_{rr} , $\sigma_{\theta\theta}$, $\sigma_{\phi\phi}$, $\sigma_{r\theta}$, and $\sigma_{\theta r}$:

$$\sigma_{rr} = \left[(\lambda + 2\mu) \frac{dc_r}{dr} + \frac{2\lambda}{r} (c_r + c_\theta) \right] \cos \theta, \quad (\text{E2a})$$

$$\sigma_{\theta\theta} = \sigma_{\phi\phi} = \left[\lambda \frac{dc_r}{dr} + \frac{2(\lambda + \mu)}{r} (c_r + c_\theta) \right] \cos \theta, \quad (\text{E2b})$$

$$\sigma_{r\theta} = \sigma_{\theta r} = \mu \left[\frac{dc_\theta}{dr} - \frac{1}{r} (c_r + c_\theta) \right] \sin \theta. \quad (\text{E2c})$$

In the absence of an external body force, the stress tensor is divergence free, and satisfies the elastostatic equilibrium conditions

$$\begin{aligned}\frac{\partial \sigma_{rr}}{\partial r} + \frac{1}{r} \frac{\partial \sigma_{r\theta}}{\partial \theta} + \frac{1}{r \sin \theta} \frac{\partial \sigma_{r\phi}}{\partial \phi} \\ + \frac{1}{r} (2\sigma_{rr} - \sigma_{\theta\theta} - \sigma_{\phi\phi} + \sigma_{r\theta} \cot \theta) = 0,\end{aligned}\quad (\text{E3a})$$

$$\begin{aligned}\frac{\partial \sigma_{r\theta}}{\partial r} + \frac{1}{r} \frac{\partial \sigma_{\theta\theta}}{\partial \theta} + \frac{1}{r \sin \theta} \frac{\partial \sigma_{\theta\phi}}{\partial \phi} \\ + \frac{1}{r} [(\sigma_{\theta\theta} - \sigma_{\phi\phi}) \cot \theta + 3\sigma_{r\theta}] = 0.\end{aligned}\quad (\text{E3b})$$

Substituting Eqs. (E2a)–(E2c) into (E3a) and (E3b), we obtain a set of coupled, linear, second-order, ordinary differential equations governing $\{c_r(r), c_\theta(r)\}$:

$$\begin{aligned}(\lambda + 2\mu) \frac{d^2 c_r}{dr^2} + \left(\frac{2(\lambda + 2\mu)}{r} \right) \frac{dc_r}{dr} + \left(\frac{2(\lambda + \mu)}{r} \right) \frac{dc_\theta}{dr} \\ - \frac{2(\lambda + 3\mu)}{r^2} (c_r + c_\theta) = 0,\end{aligned}\quad (\text{E4a})$$

$$\begin{aligned}\mu \frac{d^2 c_\theta}{dr^2} + \frac{2\mu}{r} \frac{dc_\theta}{dr} - \left(\frac{\lambda + \mu}{r} \right) \frac{dc_r}{dr} \\ - \frac{2(\lambda + 2\mu)}{r^2} (c_r + c_\theta) = 0.\end{aligned}\quad (\text{E4b})$$

The general solution to the system of ordinary differential equations is formed by the linear combinations of four linearly independent solutions. The four independent solutions can be verified by direct substitution:

$$(c_r(r), c_\theta(r)) = (1, -1), \quad (\text{E5a})$$

$$(c_r(r), c_\theta(r)) = \frac{1}{r^3} (2, 1), \quad (\text{E5b})$$

$$(c_r(r), c_\theta(r)) = r^2 (-\lambda + \mu, 2\lambda + 3\mu), \quad (\text{E5c})$$

$$(c_r(r), c_\theta(r)) = \frac{1}{r} (-2\lambda - 4\mu, \lambda + 3\mu). \quad (\text{E5d})$$

The desired solution satisfying the boundary conditions (33a) to (33d) is determined by a suitable linear combination of the four basis solutions:

$$c_r(r) = \frac{1}{\Delta} \left[F_1 + \frac{2F_2}{r^3} + F_3(-\lambda + \mu)r^2 - \frac{2F_4(\lambda + 2\mu)}{r} \right], \quad (\text{E6a})$$

$$c_\theta(r) = \frac{1}{\Delta} \left[-F_1 + \frac{F_2}{r^3} + F_3(2\lambda + 3\mu)r^2 + \frac{F_4(\lambda + 3\mu)}{r} \right], \quad (\text{E6b})$$

where Δ and F_i are algebraic expressions of the material parameters of the foam, the core displacement Z_c , and the shell displacement Z_s of the resonant unit:

$$\begin{aligned} \Delta \equiv & (R_2 - R_1) [\lambda^2 (R_2 - R_1)^2 (4R_1^2 + 7R_1R_2 + 4R_2^2) \\ & + 2\lambda\mu (13R_1^4 + 8R_1^3R_2 + 3R_1^2R_2^2 \\ & + 8R_1R_2^3 + 13R_2^4) + 5\mu^2 (8R_1^4 + 7R_1^3R_2 \\ & + 6R_1^2R_2^2 + 7R_1R_2^3 + 8R_2^4)], \quad (\text{E7a}) \end{aligned}$$

$$\begin{aligned} F_1 \equiv & 9R_1R_2(R_1 + R_2)(\lambda^2 + 4\lambda\mu + 5\mu^2)(R_1^2Z_s - R_2^2Z_c) \\ & - 2(R_1^2 + R_1R_2 + R_2^2)(\lambda + 4\mu)(2\lambda + 5\mu) \\ & \times (R_2^3Z_s - R_1^3Z_c), \quad (\text{E7b}) \end{aligned}$$

$$F_2 \equiv R_1^3R_2^3(R_1^2 + R_1R_2 + R_2^2)(\lambda + \mu)(\lambda + 4\mu)(Z_s - Z_c), \quad (\text{E7c})$$

$$F_3 \equiv 3R_1R_2(R_1 + R_2)(\lambda + \mu)(Z_s - Z_c), \quad (\text{E7d})$$

$$\begin{aligned} F_4 \equiv & 3R_1R_2(R_1^4 + R_1^3R_2 + R_1^2R_2^2 + R_2^3R_1 + R_2^4) \\ & \times (\lambda + 4\mu)(Z_s - Z_c). \quad (\text{E7e}) \end{aligned}$$

The stress tensor components σ_{rr} and $\sigma_{\theta r}$ are required to calculate the elastic restoring force acting on the core and the shell, determined by substituting Eqs. (E6a) and (E6b) into (E2a) and (E2c):

$$\begin{aligned} \sigma_{rr} = \frac{1}{\Delta} \left[-\frac{12\mu F_2}{r^4} + 2F_3\mu(3\lambda + 2\mu)r \right. \\ \left. + \frac{2F_4\mu(3\lambda + 4\mu)}{r^2} \right] \cos \theta, \quad (\text{E8a}) \end{aligned}$$

$$\sigma_{r\theta} = \sigma_{\theta r} = \frac{1}{\Delta} \left[-\frac{6\mu F_2}{r^4} + F_3\mu(3\lambda + 2\mu)r - \frac{2F_4\mu^2}{r^2} \right] \sin \theta. \quad (\text{E8b})$$

By integrating the stress tensor over the spherical boundary $\{r = R_{1/2}\}$, we calculate the force per unit length acting on the core and shell:

$$\begin{aligned} \mathbf{f}_c &= \oint_{\{r=R_1\}} \vec{\sigma} \cdot \hat{\mathbf{n}} dS = \oint_{\{r=R_1\}} (\sigma_{rr}\hat{\mathbf{r}} + \sigma_{\theta r}\hat{\boldsymbol{\theta}}) dS \\ &= \oint_{\{r=R_1\}} (\sigma_{rr} \cos \theta - \sigma_{\theta r} \sin \theta) \hat{\mathbf{z}} dS \\ &= \frac{8\pi\mu(\lambda + 2\mu)F_4}{\Delta} \hat{\mathbf{z}}, \quad (\text{E9a}) \end{aligned}$$

$$\mathbf{f}_s = \oint_{\{r=R_2\}} \vec{\sigma} \cdot \hat{\mathbf{n}} dS = -\mathbf{f}_c. \quad (\text{E9b})$$

Here, $\hat{\mathbf{n}}$ denotes a normal vector directed towards the foam region on the boundary. We have used the basis vector in spherical coordinates: $\hat{\mathbf{r}} = \sin \theta \cos \phi \hat{\mathbf{x}} + \sin \theta \sin \phi \hat{\mathbf{y}} + \cos \theta \hat{\mathbf{z}}$, $\hat{\boldsymbol{\theta}} = \cos \theta \cos \phi \hat{\mathbf{x}} + \cos \theta \sin \phi \hat{\mathbf{y}} - \sin \theta \hat{\mathbf{z}}$. Note that the internal forces cancel out in the elastostatic limit, as required by Newton's third law.

APPENDIX F: MASSES AND MOMENTS OF INERTIA OF DUMBBELL-SHAPED SOLIDS

The mass and moments of inertia of the dumbbell-shaped core and shell are calculated through studying a generic, similarly shaped dumbbell of unspecified length parameters. Consider an azimuthally symmetric dumbbell of material density ρ consisting of two spheres of common radii R , separated at a distance a between the centers where $a \geq 2R$, connected by a cylindrical handle of radius r where $r \leq R$. Suppose the axis of rotational symmetry is aligned with the z axis. The mass m_{db} , axial moment of inertia $I_{\text{db},z}$, and transversal moments of inertia $I_{\text{db},x/y}$ are determined by volume integrals over the dumbbell-shaped regions \mathcal{R}_{db} :

$$m_{\text{db}}(R, r, a, \rho) = \int_{\mathcal{R}_{\text{db}}} \rho(\mathbf{r}) dV = \rho\pi \left(\frac{4}{3}R^3 + \frac{4}{3}l^3 + ar^2 \right), \quad (\text{F1a})$$

$$I_{\text{db},z}(R, r, a, \rho) = \int_{\mathcal{R}_{\text{db}}} \rho(\mathbf{r})(x^2 + y^2) dV = \rho\pi \left(\frac{8}{15}R^5 - \frac{4}{5}l^5 + \frac{4}{3}R^2l^3 + \frac{1}{2}ar^4 \right), \quad (\text{F1b})$$

$$\begin{aligned} I_{\text{db},x}(R, r, a, \rho) = \int_{\mathcal{R}_{\text{db}}} \rho(\mathbf{r})(y^2 + z^2) dV = \rho\pi \left[\frac{12}{15}R^5 - \frac{2}{5}l^5 + \frac{2}{3}R^2l^3 + \frac{2}{3}a^2R^3 + \frac{1}{4}ar^4 \right. \\ \left. + \frac{1}{30} \left(\frac{a}{2} - l \right)^4 (a + 8l) - \frac{1}{30} \left(\frac{a}{2} - R \right)^4 (a + 8R) \right], \quad (\text{F1c}) \end{aligned}$$

where $l = \sqrt{R^2 - r^2}$ and $I_{\text{db},y} = I_{\text{db},x}$ by azimuthal symmetry.

We calculate the mass and moments of inertia of the conformally coated dumbbell. By connecting two neighboring units at fixed filling fractions, the masses of the steel core and the cellulose shell are double the values of the spherical core-shell resonators in Sec. V. These are verified by applying Eq. (F1a):

$$m_c^{(c)} = m_{\text{db}} \left(R_1^{(c)}, \frac{R_3^{(c)}}{6}, a^{(c)}, \rho_c \right) \approx 1.588 \text{ g}, \quad (\text{F2a})$$

$$m_s^{(c)} = m_{\text{db}} \left(R_3^{(c)}, \frac{R_3^{(c)}}{3}, a^{(c)}, \rho_s \right) - m_{\text{db}} \left(R_2^{(c)}, \frac{R_3^{(c)}}{4}, a^{(c)}, \rho_s \right) \approx 0.5400 \text{ g}. \quad (\text{F2b})$$

The axial moments of inertia of the core and shell are roughly double the respective values of the core and shell of the spherical resonators in Sec. V, because the axis of azimuthal symmetry passes through the centers of the two spherical caps. On the other hand, the transversal moments of inertia are an order of magnitude larger, as the masses are distributed away from the midplane of the dumbbell. The exact values are determined using Eqs. (F1b) and (F1c):

$$I_{c,z}^{(c)} = I_{\text{db},z} \left(R_1^{(c)}, \frac{R_3^{(c)}}{6}, a^{(c)}, \rho_c \right) \approx 4.886 \text{ g mm}^2, \quad (\text{F3a})$$

$$I_{c,x}^{(c)} = I_{c,y}^{(c)} = I_{\text{db},x} \left(R_1^{(c)}, \frac{R_3^{(c)}}{6}, a^{(c)}, \rho_c \right) \approx 42.83 \text{ g mm}^2, \quad (\text{F3b})$$

$$I_{s,z}^{(c)} = I_{\text{db},z} \left(R_3^{(c)}, \frac{R_3^{(c)}}{3}, a^{(c)}, \rho_s \right) - I_{\text{db},z} \left(R_2^{(c)}, \frac{R_3^{(c)}}{4}, a^{(c)}, \rho_s \right) \approx 7.586 \text{ g mm}^2, \quad (\text{F3c})$$

$$I_{s,x}^{(c)} = I_{s,y}^{(c)} = I_{\text{db},x} \left(R_3^{(c)}, \frac{R_3^{(c)}}{3}, a^{(c)}, \rho_s \right) - I_{\text{db},x} \left(R_2^{(c)}, \frac{R_3^{(c)}}{4}, a^{(c)}, \rho_s \right) \approx 21.27 \text{ g mm}^2. \quad (\text{F3d})$$

Next, we calculate the mass and moments of inertia of the connected shell dumbbell by parallel axis theorem and Eqs. (F1a)–(F1c):

$$m_s^{(f)} = m_{\text{db}} \left(R_3, \frac{R_3}{6}, a, \rho_s \right) - \frac{8\pi}{3} \rho_s R_2^5 \approx 0.5449 \text{ g}, \quad (\text{F4a})$$

$$m_{c1}^{(f)} = \frac{4\pi}{3} \rho_{c1} R_1^3 \approx 0.7940 \text{ g}, \quad (\text{F4b})$$

$$m_{c2}^{(f)} = \frac{4\pi}{3} \rho_{c2} R_1^3 \approx 0.8099 \text{ g}, \quad (\text{F4c})$$

$$I_{s,x}^{(f)} = I_{s,y}^{(f)} = I_{\text{db},x} \left(R_3, \frac{R_3}{3}, a, \rho_s \right) - \frac{16\pi}{15} \rho_s R_2^5 - \frac{2\pi}{3} \rho_s R_2^3 a^2 \approx 21.01 \text{ g mm}^2, \quad (\text{F4d})$$

$$I_{s,z}^{(f)} = I_{\text{db},z} \left(R_3, \frac{R_3}{3}, a, \rho_s \right) - \frac{16\pi}{15} \rho_s R_2^5 \approx 7.512 \text{ g mm}^2, \quad (\text{F4e})$$

$$I_{c1}^{(f)} = \frac{8\pi}{15} \rho_{c1} R_1^5 \approx 2.633 \text{ g mm}^2, \quad (\text{F4f})$$

$$I_{c2}^{(f)} = \frac{8\pi}{15} \rho_{c2} R_1^5 \approx 2.686 \text{ g mm}^2. \quad (\text{F4g})$$

-
- [1] M. S. Kushwaha, P. Halevi, L. Dobrzynski, and B. Djafari-Rouhani, *Phys. Rev. Lett.* **71**, 2022 (1993).
[2] M. S. Kushwaha, P. Halevi, G. Martínez, L. Dobrzynski, and B. Djafari-Rouhani, *Phys. Rev. B* **49**, 2313 (1994).
[3] F. R. Montero de Espinosa, E. Jiménez, and M. Torres, *Phys. Rev. Lett.* **80**, 1208 (1998).
[4] J. V. Sánchez-Pérez, D. Caballero, R. Martínez-Sala, C. Rubio, J. Sánchez-Dehesa, F. Meseguer, J. Llinares, and F. Gálvez, *Phys. Rev. Lett.* **80**, 5325 (1998).
[5] Z. Liu, X. Zhang, Y. Mao, Y. Y. Zhu, Z. Yang, C. T. Chan, and P. Sheng, *Science* **289**, 1734 (2000).
[6] N. Kaina, F. Lemoult, M. Fink, and G. Lerosey, *Nature (London)* **525**, 77 (2015).
[7] R. Süssstrunk and S. D. Huber, *Science* **349**, 47 (2015).
[8] P. Wang, L. Lu, and K. Bertoldi, *Phys. Rev. Lett.* **115**, 104302 (2015).
[9] S. H. Mousavi, A. B. Khanikaev, and Z. Wang, *Nat. Commun.* **6**, 8682 (2015).

- [10] F. Lucklum and M. J. Vellekoop, *Proc. Eng.* **120**, 1095 (2015).
- [11] F. Lucklum and M. J. Vellekoop, *IEEE Trans. Ultrason. Ferroelectr. Freq. Control* **63**, 796 (2016).
- [12] F. Lucklum and M. J. Vellekoop, *Crystals* **7**, 348 (2017).
- [13] M. Askari, D. A. Hutchins, P. J. Thomas, L. Astolfi, R. L. Watson, M. Abdi, M. Ricci, S. Laureti, L. Nie, S. Freear, R. Wildman, C. Tuck, M. Clarke, E. Woods, and A. T. Clare, *Addit. Manuf.* **36**, 101562 (2020).
- [14] F. Lucklum and M. J. Vellekoop, *Appl. Phys. Lett.* **113**, 201902 (2018).
- [15] J. A. Iglesias Martínez, J. Moughames, G. Ulliac, M. Kadic, and V. Laude, *Appl. Phys. Lett.* **118**, 063507 (2021).
- [16] K. H. Matlack, M. Serra-Garcia, A. Palermo, S. D. Huber, and C. Daraio, *Nat. Mater.* **17**, 323 (2018).
- [17] K. L. S. Yip and S. John, *Phys. Rev. B* **104**, 054302 (2021).
- [18] K. L. S. Yip and S. John, *Phys. Rev. B* **107**, L060306 (2023).
- [19] K. L. S. Yip and S. John, *Phys. Rev. B* **103**, 094304 (2021).
- [20] L. Landau, E. Lifshitz, A. Kosevich, J. Sykes, L. Pitaevskii, and W. Reid, *Theory of Elasticity: Volume 7*, Course of Theoretical Physics (Elsevier, Oxford, 1986).
- [21] Y. Pennec, J. Vasseur, B. Djafari-Rouhani, L. Dobrzynski, and P. Deymier, *Surf. Sci. Rep.* **65**, 229 (2010).
- [22] L. Li, *J. Opt. Soc. Am. A* **13**, 1870 (1996).
- [23] P. Lalanne, *Phys. Rev. B* **58**, 9801 (1998).
- [24] Y. Cao, Z. Hou, and Y. Liu, *Phys. Lett. A* **327**, 247 (2004).
- [25] M. I. Hussein, *Proc. Math. Phys. Eng.* **465**, 2825 (2009).
- [26] O. R. Bilal and M. I. Hussein, *Phys. Rev. E* **84**, 065701(R) (2011).
- [27] M. I. Hussein, M. J. Leamy, and M. Ruzzene, *Appl. Mech. Rev.* **66**, 040802 (2014).
- [28] A. S. Phani, J. Woodhouse, and N. A. Fleck, *J. Acoust. Soc. Am.* **119**, 1995 (2006).
- [29] F. Farzbod and M. J. Leamy, *J. Sound Vib.* **325**, 545 (2009).
- [30] J.-B. Li, Y.-S. Wang, and C. Zhang, *J. Comput. Acoust.* **20**, 1250014 (2012).
- [31] J.-B. Li, Y.-S. Wang, and C. Zhang, *J. Vib. Acoust.* **135**, 031015 (2013).
- [32] H.-W. Dong, X.-X. Su, Y.-S. Wang, and C. Zhang, *Struct. Multidiscip. Optim.* **50**, 593 (2014).
- [33] J. Korryng, *Physica (Amsterdam)* **13**, 392 (1947).
- [34] W. Kohn and N. Rostoker, *Phys. Rev.* **94**, 1111 (1954).
- [35] W. Jones and N. March, *Theoretical Solid State Physics*, Dover books on Physics and Chemistry, Vol. 2 (Dover, New York, 1985).
- [36] N. A. Nicorovici, R. C. McPhedran, and L. C. Botten, *Phys. Rev. E* **52**, 1135 (1995).
- [37] C. G. Poulton, A. B. Movchan, R. C. McPhedran, N. A. Nicorovici, and Y. A. Antipov, *Proc. R. Soc. London A* **456**, 2543 (2000).
- [38] S. K. Chin, N. A. Nicorovici, and R. C. McPhedran, *Phys. Rev. E* **49**, 4590 (1994).
- [39] D. Torrent and J. Sánchez-Dehesa, *New J. Phys.* **13**, 093018 (2011).
- [40] S. Nemat-Nasser, J. R. Willis, A. Srivastava, and A. V. Amirkhizi, *Phys. Rev. B* **83**, 104103 (2011).
- [41] A. N. Norris, A. L. Shuvalov, and A. A. Kutsenko, *Proc. R. Soc. A* **468**, 1629 (2012).
- [42] D. Torrent, Y. Pennec, and B. Djafari-Rouhani, *Phys. Rev. B* **92**, 174110 (2015).
- [43] J. Li and C. T. Chan, *Phys. Rev. E* **70**, 055602(R) (2004).
- [44] Y. Wu, Y. Lai, and Z.-Q. Zhang, *Phys. Rev. B* **76**, 205313 (2007).
- [45] M. M. Sigalas and C. M. Soukoulis, *Phys. Rev. B* **51**, 2780 (1995).
- [46] L. Han, Y. Zhang, Z.-Q. Ni, Z.-M. Zhang, and L.-H. Jiang, *Phys. B (Amsterdam)* **407**, 4579 (2012).
- [47] S.-H. Jo, H. Yoon, Y. C. Shin, and B. D. Youn, *Int. J. Mech. Sci.* **193**, 106160 (2021).
- [48] Y. Lu and A. Srivastava, *Wave Motion* **60**, 46 (2016).
- [49] Y. Lu and A. Srivastava, *J. Mech. Phys. Solids* **111**, 100 (2018).
- [50] A. Y.-T. Leung, *Int. J. Numer. Meth. Eng.* **12**, 1705 (1978).
- [51] L. E. Suarez and M. P. Singh, *AIAA J.* **30**, 1046 (1992).
- [52] Y.-B. Yang and B.-H. Lin, *J. Struct. Eng.* **121**, 1636 (1995).
- [53] A. Cea and R. Palacios, *J. Fluids Struct.* **101**, 103222 (2021).
- [54] J. Carvill, *Mechanical Engineer's Data Handbook* (Butterworth-Heinemann, Oxford, 1993).
- [55] B. Moore, T. Jaglinski, D. Stone, and R. Lakes, *Cellular Poly.* **26**, 1 (2007).
- [56] G. F. Bassani and G. P. Parravicini, *Electronic States and Optical Transitions in Solids*, International Series of Monographs in the Science of the Solid State (Pergamon Press, Oxford, 1975).
- [57] Y. Lu, Y. Yang, J. K. Guest, and A. Srivastava, *Sci. Rep.* **7**, 1 (2017).
- [58] H. C. Wilcox, *J. Elast.* **9**, 221 (1979).
- [59] H. M. Ledbetter, N. V. Frederick, and M. W. Austin, *J. Appl. Phys.* **51**, 305 (1980).
- [60] A. Chutinan and S. John, *Phys. Rev. A* **78**, 023825 (2008).
- [61] S. Eyderman, A. Deinega, and S. John, *J. Mater. Chem. A* **2**, 761 (2014).
- [62] S. Foster and S. John, *J. Appl. Phys.* **120**, 103103 (2016).
- [63] W. R. Schowalter, *Mechanics of Non-Newtonian Fluids* (Pergamon Press, Oxford, 1978).
- [64] R. Lehoucq, D. Sorensen, and C. Yang, *ARPACK Users' Guide: Solution of Large-scale Eigenvalue Problems with Implicitly Restarted Arnoldi Methods*, Software, Environments, Tools (Society for Industrial and Applied Mathematics, Philadelphia, 1998).
- [65] M. Abramowitz and I. A. Stegun, in *Handbook of Mathematical Functions with Formulas, Graphs, and Mathematical Tables*, 10th ed. (Dover, New York, 1964), p. 363.